University of Arkansas, Fayetteville

ScholarWorks@UARK

Graduate Theses and Dissertations

8-2022

XPS and IPE Determination of Band Offsets of Germanium Based Materials

Justin Michael Rudie
University of Arkansas, Fayetteville

Follow this and additional works at: https://scholarworks.uark.edu/etd

Part of the Semiconductor and Optical Materials Commons, and the Structural Materials Commons

Citation

Rudie, J. M. (2022). XPS and IPE Determination of Band Offsets of Germanium Based Materials. *Graduate Theses and Dissertations* Retrieved from https://scholarworks.uark.edu/etd/4575

This Thesis is brought to you for free and open access by ScholarWorks@UARK. It has been accepted for inclusion in Graduate Theses and Dissertations by an authorized administrator of ScholarWorks@UARK. For more information, please contact uarepos@uark.edu.

XPS and IPE Determination of Band Offsets of Germanium Based Materials

A thesis submitted in partial fulfillment
of the requirements for the degree of
Master of Science in Materials Engineering

by

Justin Rudie
Minnesota State University Mankato
Bachelor of Science in Engineering with Electrical Emphasis, 2019

August 2022
University of Arkansas

This thesis is approved for recommendation to the Graduate Council.

Shui-Qing Yu, Ph,D.
Thesis Director

Gregory Salamo, Ph.D.
Committee Member

Morgan Ware, Ph.D.
Committee Member

Matthew Leftwich, Ph.D.
Ex-Officio Member

Timothy Morgan, Ph.D.
Ex-Officio Member

The following signatories attest that all software used in this thesis was legally licensed for use by Justin M. Rudie for research purposes and publication.

Mr. Justin Rudie, Student

Shui-Qing Yu, Thesis Director

This thesis was submitted to http://www.turnitin.com for plagiarism review by the TurnItIn company's software. The signatories have examined the report on this thesis that was returned by TurnItIn and attest that, in their opinion, the items highlighted by the software are incidental to common usage and are not plagiarized material.

Matthew Leftwich, Program Director

Shui-Qing Yu, Thesis Director

Abstract

Germanium tin and silicon germanium tin are group IV semiconductor alloys that have gained significant interest in recent years for their potential use in optoelectrical devices. While silicon and germanium are indirect bandgap materials on their own, alloying them with tin in sufficient quantities leads to a transition to direct bandgap alloys. Direct gap performance opens the door for efficient light emitting and detecting devices fabricated entirely on group IV materials that are compatible with the industry standard CMOS manufacturing techniques. Germanium tin and silicon germanium tin have bandgaps that respond to light in the mid to near infrared spectrum which is ideal for night vison technologies.

In this thesis two techniques are used to determine the band offsets of GeSn and SiGeSn heterojunctions. X-ray photoelectron spectroscopy is used to directly measure the electron binding energies at the surface of a material and these binding energies are used to determine the relative positions of the valance band maximums. The second technique is internal photon emission which relies on fabricating a photodiode device on a SiGeSn/GeSn sample and measuring the photocurrent. From the photocurrent the potential barrier heights, when photocurrent first starts to flow, can be determined and the band structure and offsets can be determined.

Knowing the band structure of semiconductor materials is crucial because the behavior of devices fabricated on these materials will have their performance determined largely by the physics at the material interfaces. Device modeling and prediction is largely reliant on having accurate band structure information. Being able model devices made on these emerging materials will be informative and guide the growth effort to focus on material compositions that are best suited for specific applications.

The sample selection criteria for the x-ray photoelectron spectroscopy and internal photon emission measurements. This will include the sample preparation necessary for the spectroscopy samples as well as the device fabrication process used to make the photodetector device for the internal photon emission measurements. Alternative band offset techniques and their merits and challenges will also be covered. The discussion concludes with an evaluation of the reliability of the measured offsets and how they compare to theoretical values and empirical values from literature. Finally, there will be plans for future work including additional offset measurements that are planned to cover a larger portion of the vast array of material composition combination for these alloys. The future work discussion will also cover the next steps for using the measured offset values for the purpose of device modeling and simulation for the realization of detectors and infrared cameras build on these group IV alloy material systems.

Contents

Chapter 1 Introduction and Background ... 1
1.1 SiGeSn & GeSn Material Overview ... 1
1.2 Motivation ... 5
1.3 Existing SiGeSn Band Offset Values Overview ... 11
1.3.1 Theoretical Results of SiGeSn Band Offsets ... 11
1.4 Organization ... 13
Chapter 2 – Survey of Band Offset Measurement Techniques ... 16
2.1 Offset Measurement Techniques Overview ... 16
2.2 IPE ... 25
2.2.1 IPE Theory ... 26
2.2.2 IPE Equipment Setup ... 28
2.3 XPS ... 29
2.3.1 XPS Theory ... 29
2.3.2 XPS Equipment Setup ... 34
Chapter 3 XPS Heterostructure Measurements ... 38
3.1 Sample Selection and Preparation ... 38
3.2 Calibration Measurements ... 41
3.3 GeSn Results and Discussion ... 46
Chapter 4 IPE Heterostructure Measurements ... 50
4.1 Sample Design and Considerations ... 50
4.2 Device Fabrication ... 51
4.3 Construction of Unique IPE Testing Setup ... 54
4.4 Results and Discussion ... 56
Chapter 5 Conclusions & Future Work ... 59
5.1 Conclusions ... 59
5.2 Future Work ... 60
Bibliography ... 62

List of Figures

Figure 1 - Simplified diagram of photoemission from both a direct and indirect band gap2

Figure 2 - Transition of GeSn from indirect to direct bandgap with increasing Sn composition. The insets show the relative change of the gamma and L valleys post-transition ....**Error! Bookmark not defined.**

Figure 3- Depiction of the alloy combinations of Si, Ge, and Sn. Alloys that have been successfully grown are indicated by points on the triangle. The growth technique used is determined by the color of the points and the shape indicates the type of alloy grown. 6

Figure 4 - Energy band diagram of two dissimilar materials being brought into contact thus forming a heterojunction. The Fermi energy level shift to be continuous through the material causing all other band energies to shift as well. 8

Figure 5 - The three types of semi-conductor heterojunction band structures 9

Figure 6 - AC bias voltage and swept DC voltage vs. time which models the sweep that would be used to conduct C-V measurements. 16

Figure 7 - The plotted voltage bias vs inverse capacitance squared values form a clear linear region. This region is extrapolated to the x-axis and the intersection represents the built-in voltage which is analogous to the CBO. Graph obtained from [30]. 17

Figure 8- a) The PL peaks from the emission of photons across the AlGaAsSb band gap (type I) and emission from the conduction band of InP to the valance band of AlGaAsSb (Type II) for different amounts of Al incorporation. b) The varying PL emission of type I and II as the Al concentration varied from 0 to ~17%. c) The VBO (black dots) and CBO (white dots) for the range of Al incorporation calculated by subtracting the type II emission from the band gap of InP and AlGaAsSb respectively. Figures from [33]. 19

Figure 9 - a) the tunneling current vs applied voltage b) the conductance vs applied voltage c) the probe distance from the surface as applied voltage changes d) the differential conductance with a stationary tip as voltage varies e) the normalized capacitance with respect to the changing voltage. Figures from [36].............................. 21

Figure 10 - Schematic of IPE measurement and plot of quantum yield vs photon energy. Distant linear regions show when excitation energy changes the dominant generated photocurrent to change from excitation across the heterojunction to excitation across the bandgap of the larger bandgap material. Figure from [41] 24

Figure 11- a) and b) show simplified energy diagrams of electrons in core level binding states of generic atoms. c shows the resulting XPS spectra with KE as the x-axis showing that the electron with larger binding energy BE2 has lower KE than BE1. 30

Figure 12- Measurement of the valance band edge of a Ge sample. The red portion represents the fit of the linear leading edge which is extrapolated to the noise floor. The intercept of these lines is the maximum of the valance band. 32

Figure 13 - a) is a cylindrical mirror analyzer showing the trajectory of electrons from sample to detector. b) is a hemispherical sector analyzer with attached lenses that retard electrons before they reach the detector .Figure from[37]. 36

Figure 14 - Core level XPS spectra for ASM-0016. Upper left is Sn core level energies in the thick GeSn layer and bottom left is Ge 3d core level energy in thick Ge and in thick GeSn for comparison to show the shift in core level energy. Upper right is the Sn core levels in the interface sample and lower right is the Ge 3d core level in the interface sample both at different stages of sputtering. 47

Figure 15 – VBE XPS spectra for thick Ge and GeSn layers of ASM-0016.................... 48

Figure 16 - Structure of sample FDY-0106 as revealed by SIMs. The red and green layers represent the two sides of the measured heterojunction. 51

Figure 17- FDY 0106 post fabrication. a) shows the chip wire bonded to the chip holder used to interface with the cryostat used for the photocurrent measurements. b) shows some of the lower quality devices fabricated on the sample. c) shows one of the high-quality devices. d) is a image of the wire bonded device used for the IPE measurments. 53

Figure 18- The IPE testing set up, a tunable 3um laser is used with an optical path to excite the sample in a cryostat which the signal is also measured by a power meter and a detector in a FTIR. 55

Figure 19 - IPE spectra of FDY-0106 at various bias voltages at 77K............................. 57

List of Tables

Table 1- Summary of theoretical band offsets between group IV materials. A back slash separates the two sides of each heterojunction and separates the atomic compositions in the Si%, Ge% and Sn% columns. 13

Table 2- Ge/GaAs XPS values 43

Table 3 - Ge/Si as well as pure Ge substrate XPS core level and core level to VBM separation values 44

Table 4 - XPS determined core level and VBE separation energies for ASM-0016 48

Chapter 1 Introduction and Background

In the field of electronics and optoelectronic devices there has been considerable interest in the group IV alloys germanium-tin ($Ge_{1-x}Sn_x$) and silicon germanium tin (SiGeSn) due to the materials' unique ability to become direct bandgap with Sn incorporation, their tunability and their compatibility with silicon.

1.1 SiGeSn & GeSn Material Overview

Silicon (Si) and germanium (Ge) both have a long history of use in semiconductor devices. The first transistor was made on Ge in 1947, but Si soon became the staple material due to its abundance and intrinsic material properties.[1] Despite Si's dominance of the semiconductor industry it is not without limitations. Especially in the field of photonics and optoelectronics the performance of both Si and Ge suffer from being indirect bandgap materials.[2] Indirect bandgap materials are defined by having a valance band maximum (VBM) and conduction band minimum (CBM) at different positions in the Brillouin zone, so they are not aligned vertically. By comparison direct bandgap materials have their CBM directly above the VBM, typically in the gamma valley of the Brillouin zone. During photoemission an electron transitions from the CBM to the VBM and a photon is emitted. As figure 1 shows photoemission in a direct transition only requires an electron hole pair while indirect transition requires a phonon particle to maintain momentum conservation.[3]

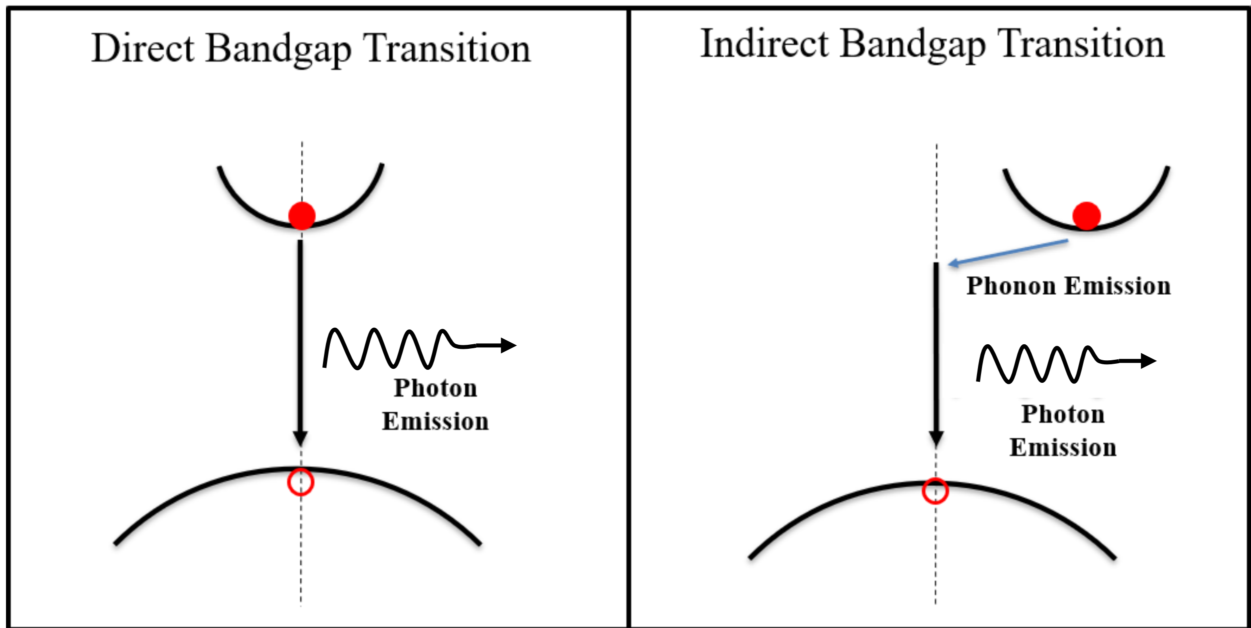

Figure 1 - Simplified diagram of photoemission from both a direct and indirect band gap

The resulting indirect transition is significantly weaker since much of the energy is lost to the phonon particle rather than all the energy being emitted as only a photon in the case of direct transitions. This makes indirect semiconductor materials very inefficient at emitting light and thus poorly suited for photonics and optoelectronic applications.

Different avenues have been explored to work around this indirect bandgap issue and develop silicon photonics because of Si's importance in the semiconductor world. One common technique is directly growing or wafer bonding direct bandgap materials such as III-V materials onto Si wafers[4]. Placing III-V materials on Si offers the benefit of strong efficient light emission from a direct bandgap material paired with a Si platform. Of course, this technique comes with its own share of challenges such has high temperatures needed for wafer bonding, large lattice constant mismatches and general scaling issues when trying to produce in large quantities.[5][6] Recently the development of two group IV semiconductor alloys have been gaining significant interest due to their potential to allow for development of direct bandgap

photonics on a monolithic Si platform. Germanium tin (GeSn) and silicon germanium tin (SiGeSn) are group IV alloys that have numerous unique material properties and potential optoelectronics application.

While direct bandgap devices on pure Si or Ge cannot be achieved, GeSn and SiGeSn alloys have the unique property of transitioning from indirect to direct bandgap with an appropriate amount of tin incorporation. As figure 2 illustrates the L valley of the conduction band is originally lower in germanium and thus closer to the VBM resulting in indirect transitions being dominate in the material. When the fraction of Sn is increased the gamma (Γ) valley of the conduction band is pulled down more quickly than the L valley. At a given temperature and compressive strain within the alloy the direct transition becomes dominate when the Sn composition reaches ~10%.[7] This allows for an entirely group IV material system that is direct bandgap, can be grown directly on Si and is compatible with the industry standard complementary metal-oxide semiconductor (CMOS) fabrication techniques.

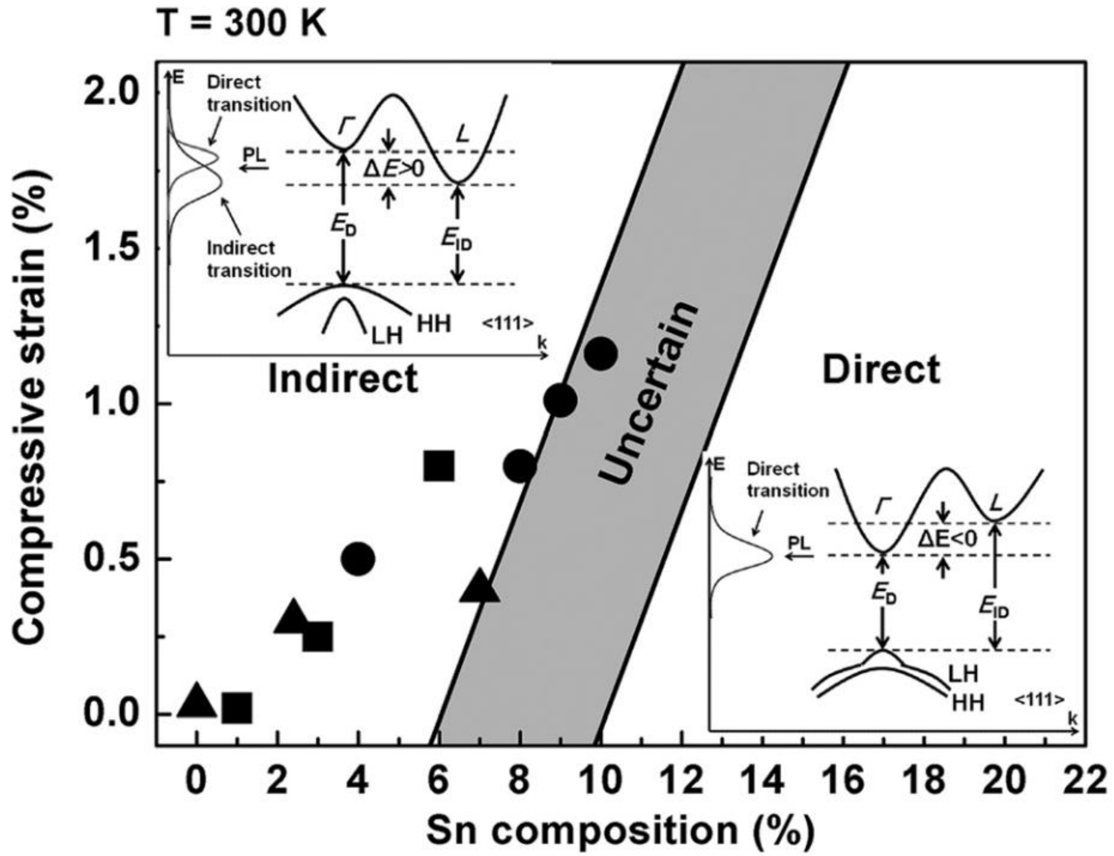

Figure 2 - Transition of GeSn from indirect to direct bandgap with increasing Sn composition. The insets show the relative change of the gamma and L valleys post-transition. The different shapes reflect the growth technique used for the growth.

The incorporation of tin in these alloys not only converts the alloys from indirect to direct transitions, but also allows for tunning of the values of the material bandgap. Near room temperature Ge has a bandgap of ~0.67 eV which decreases as it is alloyed with Sn. It has been demonstrated that increasing Sn content continues to reduce the bandgap to the extent that GeSn will transition from an indirect bandgap to a direct bandgap and alloying additional Sn can theoretically reduce the bandgap to zero.[8] This tunability is very useful for developing alloys that respond to different frequencies of light.

$$(1)\ \lambda = \frac{1240\ \text{eV*nm}}{E_g}$$

As equation 1 shows the wavelength of light that a material absorbs or emits (λ) is inversely proportional to the size of the bandgap (E_g). Materials with larger bandgap will respond to light with a shorter wavelength (higher frequency) while smaller bandgap material will respond to longer wavelength light (lower frequency). A bandgap of 0.67 eV in pure germanium corresponds to a wavelength near 1.8 µm and tuning with Sn incorporation offers the potential to cover wavelengths up to 12 µm.[9] This range covers a large portion of the near and mid-infrared (IR) spectrum of light., which has various applications for gas sensing, telecommunication and night vision technologies.[10]–[12] The potential of these bandgap tunable, Si and CMOS process compatible alloys is vast and thus a strong effort is being made to further develop the quality and understanding of these materials.

1.2 Motivation

There has been a considerable amount of progress towards developing and understanding GeSn and SiGeSn materials yet there are still challenges to overcome and knowledge that must be gleaned before these alloys can be developed into high quality devices on a large scale. From the material growth perspective innovative techniques have been developed and continued to be improved to grow higher quality GeSn and SiGeSn materials with higher Sn content, which allows for further bandgap tuning. One challenge is the tendency for tin to segregate out during growth due to the low solubility equilibrium of tin in germanium.[13] The large lattice mismatch between Ge and Sn is another challenge. The mismatch has been reported to be as large as 16%, which leads to defects forming during growth thus reducing material quality.[14], [15]. The lattice mismatch of Ge and Si is also fairly large with Ge's lattice constant being 4.2% larger than Si's and Sn incorporation increases this mismatch. To avoid defects from strain due to

these large lattice constant differences, specific growth techniques and recipes must be used to avoid excessive strain during sample growth.[16] Different growth techniques including molecular beam epitaxy (MBE) and chemical vapor deposition (CVD) and sputtering epitaxy have been employed to solve these growth challenges with innovative methods such as higher order precursor gases, buffer layers and low temperature growth techniques.[17]–[21]

Despite these innovative techniques there is a vast number of possible composition combinations for GeSn and SiGeSn alloys and as figure 3 shows, only a few have been realized.

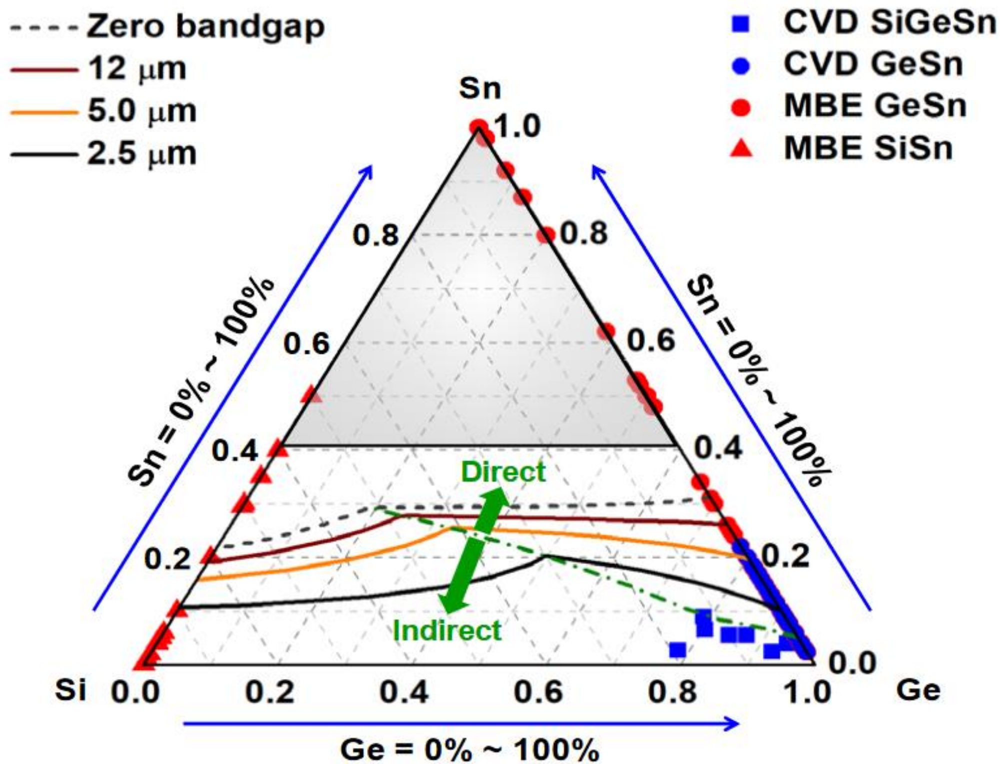

Figure 3- Depiction of the alloy combinations of Si, Ge, and Sn. Alloys that have been successfully grown are indicated by points on the triangle. The growth technique used is determined by the color of the points and the shape indicates the type of alloy grown.

As these alloys growth techniques continue to improve and more alloy compositions are realized, it is important that the key material parameters of these alloys that are necessary for the development of advanced electrical and optoelectrical devices are determined and understood in parallel. Today many semiconductor structures, which would otherwise be unobtainable with simple homojunction interfaces, are based on heterojunction interfaces [22] A semiconductor heterojunction is the interface at the joining of two dissimilar materials which have unequal energy bandgaps, as opposed to homojunctions which are formed by materials with the same bandgap on either side of their interface. Two of the most important characteristics that define a heterojunction are the valance band offset (VBO) and conduction band offset (CBO).[22] These offsets are defined as the discontinuity of the band edge at the interface, the VBO being the discontinuity of the valance band maximum (VBM) and the CBO the discontinuity of the conduction band minimum of the joined materials.[22] These are important values because they determine the offset type and band structure. As figure 5 shows this creates the potential barriers that will confine holes and electrons and the size of the offset is proportional to the strength of the confinement.

Band offsets occur at a heterojunction in order for the Fermi energy to remain continuous throughout the semi-conductor. As figure 4 shows once two materials are brough into contact the

Femi energy levels will shift in order to align, shifting all other energy levels by the same amount in the process.

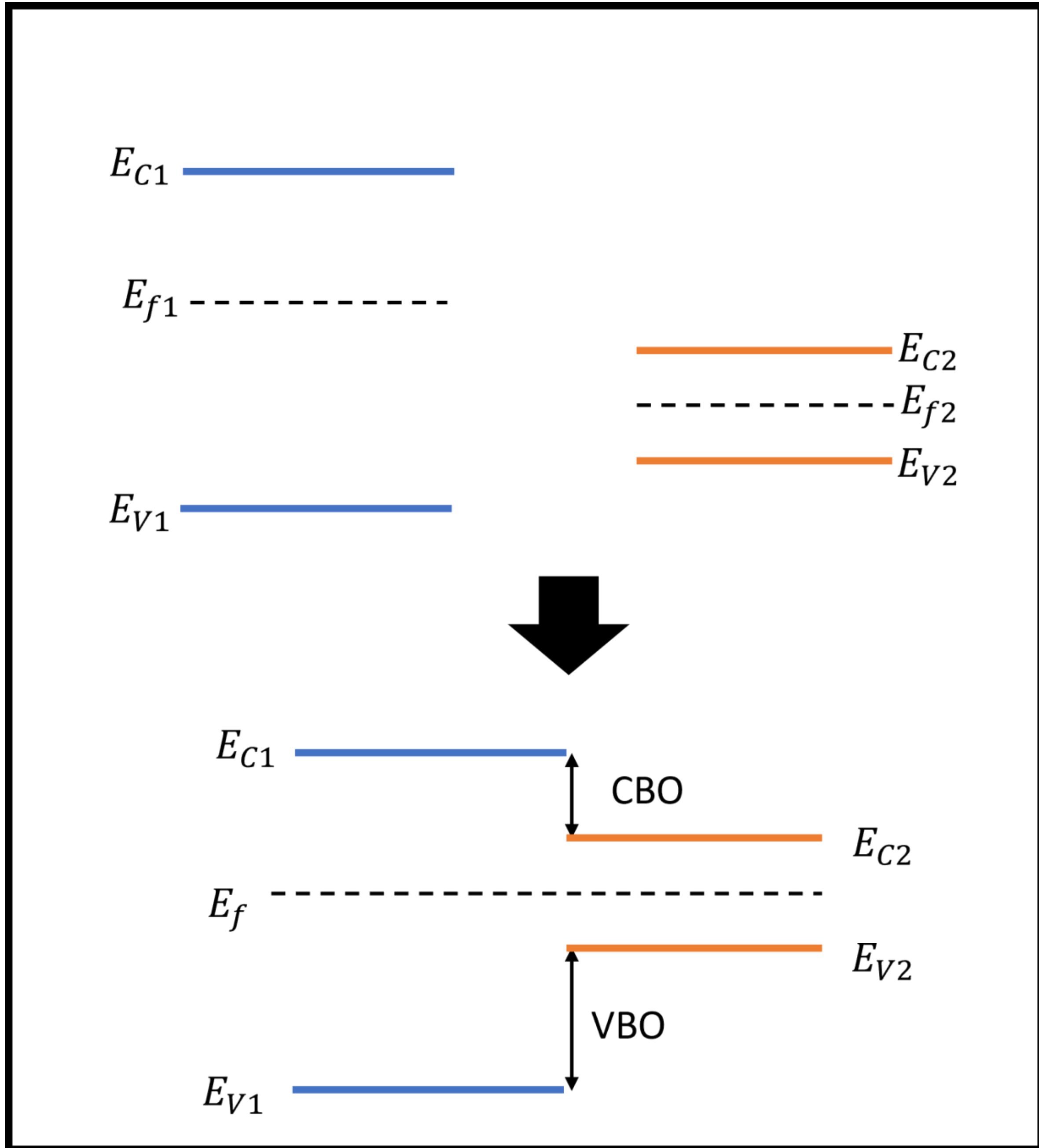

Figure 4 - Energy band diagram of two dissimilar materials being brought into contact thus forming a heterojunction. The Fermi energy level shift to be continuous through the material causing all other band energies to shift as well.

This shift can result in different energy band structures that effectively determine the behavior of resulting devices fabricated with these material interfaces. There are three types of band structures that can occur when two dissimilar materials meet as shown in figure 5. Type I structures occur when the smaller bandgap material has a CBM lower than the larger bandgap material and a VBM higher than the larger bandgap material. The type II structure occurs when one material has both its CBM and VBM lower than the corresponding energy bands of the second material. The third structure, the type III band structure is defined by one material having both its VBM and CBM below the VBM of the second material.[22]

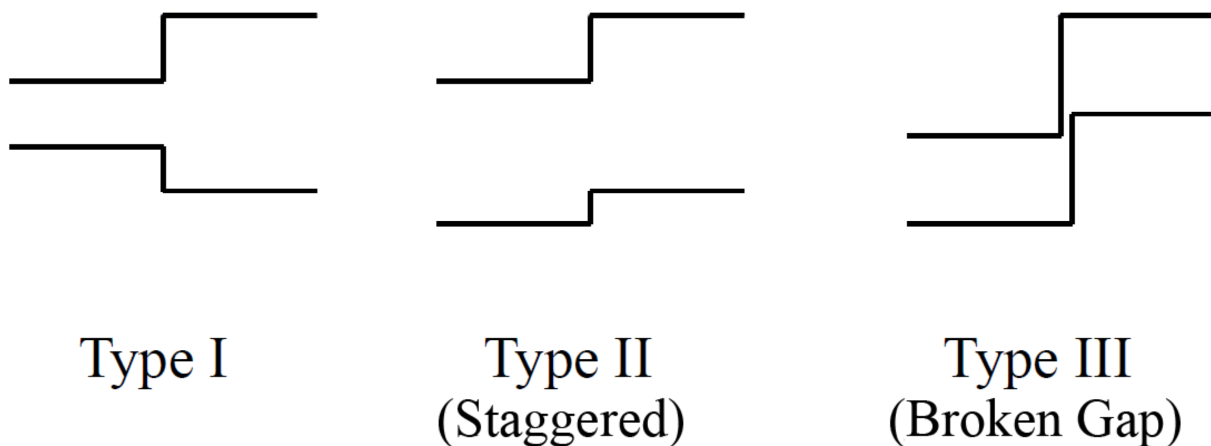

Figure 5 - The three types of semi-conductor heterojunction band structures

This energy structure has a large impact on charge carrier separation and confinement. The VBO and CBO serve as potential barriers to confine electrons and holes which can increase the carrier lifetimes.[23] To effectively predict and model carrier confinement that will determine the performance of resulting devices, it is prudent to accurately know how the alignment type and the magnitude of the offsets

Knowing the CBO and VBO is very valuable information, but determining these values is

not a trivial task. Both empirical and theoretical approaches have been proposed and demonstrated to find the offsets of semiconductor heterojunctions, but they are not without their limitations and considerations. Early theoretical models used simple predictions such as the Anderson model which assumed that the CBO was the difference between the measured electron affinities of the constituent materials that form the heterojunction. This does not take into the chemical bonding effects that may result in defect states, electrical polarization of the interface states, or the effects of dislocations and other lattice imperfections at the interface. [22] Other techniques have attempted to relate the offsets to empirically measured properties of the heterojunction interface and some models have been made purely based on theoretical values. Neither of these approaches are completely reliable as a complete understanding of the physics of band offsets has not yet been realized.[22] In order to be of practical use for modeling and design of semiconductor devices which can have small offsets on the order of a few tenths of an electron volt these offsets must be determined with a accuracy smaller than ±0.10 eV. Unfortunately many predictive models span a range of more than 1 eV.[22] Thus direct empirical measurements are necessary for reliable band offset information.

Even among empirical methods the technical difficulties and sometimes indirect nature of the measurement calls into question the reliability of the determined offsets. Some results have indicated that the offset values are heavily influenced by the conditions in which the interface was prepared and without knowing exactly what factors influence the offsets it is difficult to reliably reproduce these offset measurements.[22] Yet many empirical methods have been developed which have determined the offsets of a large number of heterojunctions with fairly reliable accuracy. These experimental methods can largely be grouped into three categories. The first are optical spectroscopy techniques which analyze absorption, photoluminescence or photoluminescence excitation spectra data and determine the offsets as fitted parameters.[22]

The next are electron spectroscopy techniques that can directly measure the VBO. [22] Third are electrical techniques that make use of devices fabricated on the material to measure conduction-voltage (C-V) or current-voltage (I-V) relationships and extract the offsets from this data.[22] A brief overview of a few of these methods will be discussed in section 2.1.

1.3 Existing SiGeSn Band Offset Values Overview

As previously stated, the high interest in the GeSn and SiGeSn material systems has motivated considerable efforts to develop and understand these alloys. Both empirical and theoretical experiments have been performed and a short overview of some of these findings will be covered here.

1.3.1 Theoretical Results of SiGeSn Band Offsets

Although theoretical results of calculated band offsets tend to be less reliable, even in the case where the accuracy is on the order of ± 1 eV these values may provide insight at least into the band alignment type. These theoretical values can be useful when empirical measurements are made and need something to check against for confirming the results, even if it’s a rough form of verification. One method for determining the offsets in a heterojunction is a model developed by Jaros in 1988 and is often referred to by his namesake. Jaros’ model uses measured values of the optical dielectric constants and the lattice constants of the constituent materials to find the resulting VBO of a heterojunction, the CBO can then be determined if the bandgaps of the constituent materials are known.[24] This model results in an equation that determines the

energy of the average valance band of the SiGeSn or GeSn alloy relative to the average valance band energy of the material on the other side of the heterojunction interface.

In many cases researchers calculated this VBO with respect to the average valance band energy of Ge. For example, Chang, Sun, and Menéndez all used approximately the same equation $\Delta E_{v,av}$ = -0.48x+0.69y to determine the VBO over the range of compositions they modeled. [25]–[27] Here $\Delta E_{v,av}$ the difference in valance band energies is determined by the amount of Si (x) and Sn (y) in the SiGeSn alloy. Menéndez and Chang modeled the $Ge/Si_xGe_{1-x-y}Sn_y$ interface, with Chang focusing on a $Si_{0.05}Ge_{0.75}Sn_{0.2}$ QW laser grown on Ge while Menéndez modeled a range of compositions from 10-40% Sn while keeping the Si content constant at 15%.[26], [27] Based on the compositions Chang's VBO was ~0.14 eV with the SiGeSn VBM above Ge's VBM.[26] Menéndez's offsets spanned a range from -0.003 – 0.2 eV as the Sn composition was increased from 10-40%. [27] Sun modeled an injection laser where the $Ge_{0.94}Sn_{0.06}$ active region was sandwiched between two $Si_xGe_{1-x-y}Sn_y$ layers with 15% Si and Sn content that varied from 6-20% for a range of VBO from 0.04 – 0.066 eV [25]

Table 1- Summary of theoretical band offsets between group IV materials. A back slash separates the two sides of each heterojunction and separates the atomic compositions in the Si%, Ge% and Sn% columns.

Heterojunction	**Si %**	**Ge %**	**Sn %**	**VBO (eV)**	**CBO (eV)**	**Technique**	**Source**
Ge/SiGeSn	4-19	69-92	4-12	0.05	0.05	Jaros Method	[28]
GeSn/$Si_x Ge_{1-x-y} Sn_y$	0/15	94/75	6/10	-0.48x+0.69y	-	Jaros Method	[25]
Ge/$Si_x Ge_{1-x-y} Sn_y$	5	75	20	-0.47x+0.69y	-	Jaros Method	[26]
Ge/$Si_x Ge_{1-x-y} Sn_y$	15	45-75	10-40	-0.48x+0.69y	-	Jaros Method	[27]
$Si_x Ge_y Sn_{1-x-y}$/ GeSn	0-40	>20	0-40	1.17x+0.69y	-	Jaros Method	[29]

1.4 Organization

This thesis will be structured as follows. First, in chapter 2 an overview of many of the known techniques for determining band offset values in semiconductor materials will be briefly covered. The strengths, shortcomings and appropriateness of each technique will be discussed as it relates to this work. This is followed by a short justification as to why IPE and XPS were chosen as the primary characterization techniques used for the measurements.

Chapter 2 will continue with a deeper discussion of IPE and the underlying theory that governs the technique. The particularities of the method used to determine the band offsets in this work will also be covered. Next the experimental setup for the IPE measurements will be discussed in detail, including design considerations and setup validation techniques. This will be followed by an overview of existing IPE measurements from literature that were made to determine band offsets to further exemplify the merit of the technique.

The final portion of chapter 2 will include detailed discussion of the XPS measurement technique similar to how IPE was addressed. The working theory behind XPS will be covered in detail and specifics of the technique used to find the band offsets based on these measured values will be explained. There will be an overview of the equipment used to perform the measurement and prepare the samples beforehand. Finally, there will be an overview from literature of the different interfaces that have been characterized by XPS to assert the reliability of the technique.

Chapter 3 will discuss the various material characterization techniques that were used to determine the exact layer structures of the samples used in the band offset measurements. This will include a very brief overview of the technique itself and the parameter(s) of interest, such as thickness or composition, that were determined.

Following this chapter 4 will cover the empirical work related to conducting the XPS band offset measurements as well as relevant results. First sample selection and preparation steps will be discussed as well as the results of the characterization used to confirm the structure of the samples. Next will be a discussion of measurements performed on the well-known Ge and Si heterojunction which acted as calibration to confirm the technique was reliable. Finally, the results to date on the interface between GeSn and Ge will be presented.

In chapter 5 a similar discussion will be had for IPE. Just as in chapter 4, this chapter will start with explaining the criteria for sample selection and design as well as the characterization

performed to confirm the sample composition. Next there will be a section discussing the fabrication process used to make the devices that were measured by IPE. Following this is an explanation of the IPE setup and how it was constructed and tested to confirm it operated as intended. The chapter will end with a discussion of the results to date from the IPE measurements.

In the final chapter, chapter 6, there will be a summary of the conclusions that can be drawn from the measurements to date. Discussion of the confidence of the results and how they compare to existing results and theory will be addressed. Finally, there will be a section proposing the continuation of this work for the future. This includes additional samples of interest to be measured as well as the long-term next steps where the band offset values may be leveraged for device modeling and simulation.

Chapter 2 – Survey of Band Offset Measurement Techniques

2.1 Offset Measurement Techniques Overview

As stated in section 1.2 there are numerous empirical methods to measure the band offsets of heterojunctions and they can broadly be grouped into three categories. The first are electrical measurements also known as transport methods, make use of the C-V and I-V relationships of a device fabricated on the semiconductor heterojunction to determine the offsets. These are one of the oldest types of band offset measurement techniques dating back to the 1980s.[30] These measurements are performed by applying a fixed AC voltage along with a sweeping DC voltage, as shown in figure 6, across a semiconductor device while the capacitance is measured.

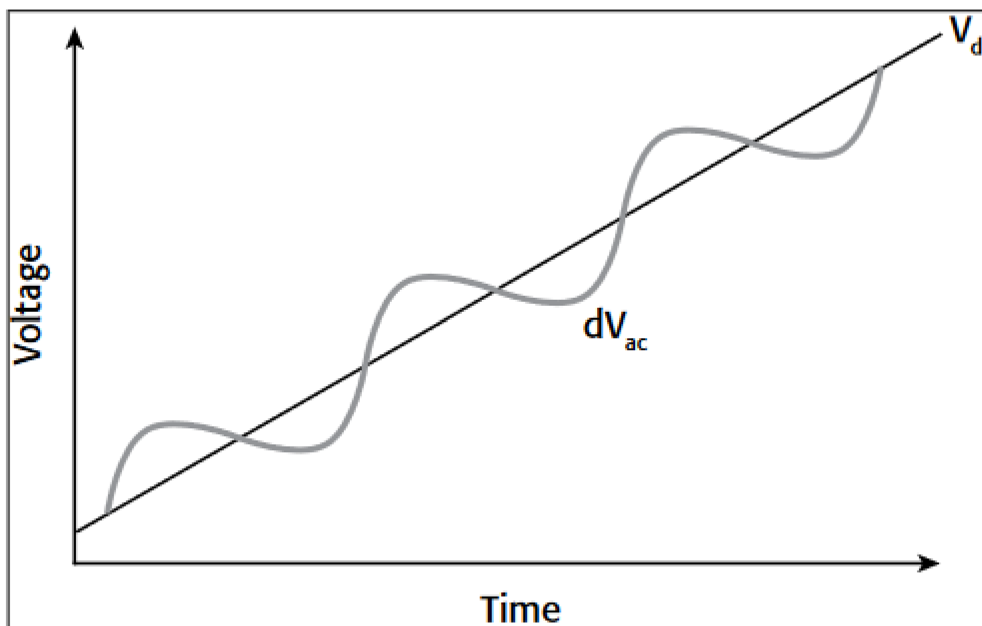

Figure 6 - AC bias voltage and swept DC voltage vs. time which models the sweep that would be used to conduct C-V measurements.

The swept DC voltage allows for sampling at different depths into a device while the consistent AC bias voltage creates the signal bias so the capacitance of the device can be measured at the given depth in the device. When the applied voltage is plotted against the squared inverse capacitance ($1/C^2$) a straight line will be generated. Linearly extrapolating this strait line to the point where it intersects with the x-axis as shown in figure 7 for graphene on Si and graphene on GaAs from TONGAY et al, will determine the built-in voltage V_{bi} for the heterojunction.[31], [32]

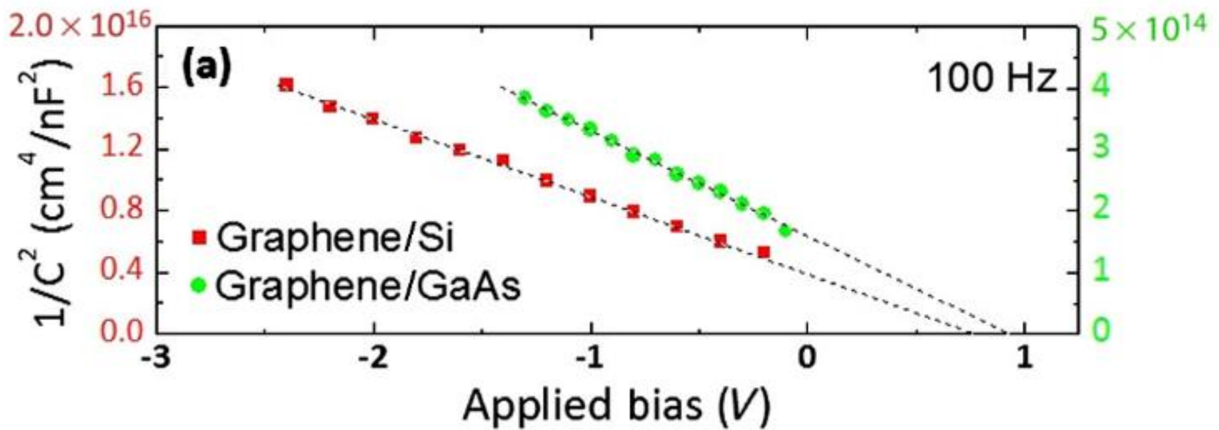

Figure 7 - The plotted voltage bias vs inverse capacitance squared values form a clear linear region. This region is extrapolated to the x-axis and the intersection represents the built-in voltage which is analogous to the CBO. Graph obtained from [32].

For heterojunctions with known constant doping in each layer this voltage will be equal to the conduction band offset of the interface. [31] This technique for band offset determination has been in use for a very long time and thus has been widely used to determine the offsets of many heterojunctions including: GaAs/AlGaAs, InGaAsP/InP, InAlAs/InGaAs, InAs/AsSb, InAsSb/GaSb and CdS/InP.[31]

Another set of techniques that have a long history of being used to determine band offsets are photoluminescence (PL) techniques. These techniques rely on analyzing the optical absorption spectra of a material to find band structure information.[33] Photoluminescence is a technique in which a semiconductor material is excited by a light source that provides photons with energy in excess of the material's bandgap. After excitation energy is absorbed by an electron in the material's valance band, it will be excited to the conduction band of the material. The excited electron will eventually relax and drop back down to the valance band, at which point it will release a photon. The energy of the emitted photons is measured with respect to the excitation energy to form a spectra that gives insight into the material's band structure properties. [34]

There are many different methods to discern the band offsets using PL and other spectrum measurements. Ostinelli measured the PL emission from the interface between InP and $Al_xGa_{1-x}AsSb$ with Al concentrations ranging from 0 to 17 percent. The resulting PL spectra had distinct peaks for the type I emission from recombination across the AlGaAsSb bandgap and the type II emission from recombination from the conduction band of InP to the valance band of AlGaAsSb as seen in figure 8a**.** [35] The type I and Type II emission was measured for varying Al content up to nearly 17% and it can be seen in figure 8b that both emissions increased with increasing Al content alluding to bandgap widening. From the bandgap values and the type II PL emissions it was possible to calculate the CBO and VBO at any amount of Al incorporation by simple subtraction. Subtracting the type II emission from the InP gap (which was measured by low temp PL at 15 K) resulted in the VBO. Similarly, subtracting the type II emission from the $Al_xGa_{1-x}AsSb$ at the corresponding Al incorporation resulted in the CBO and these offset energies were plotted in figure 8c**.**[35]

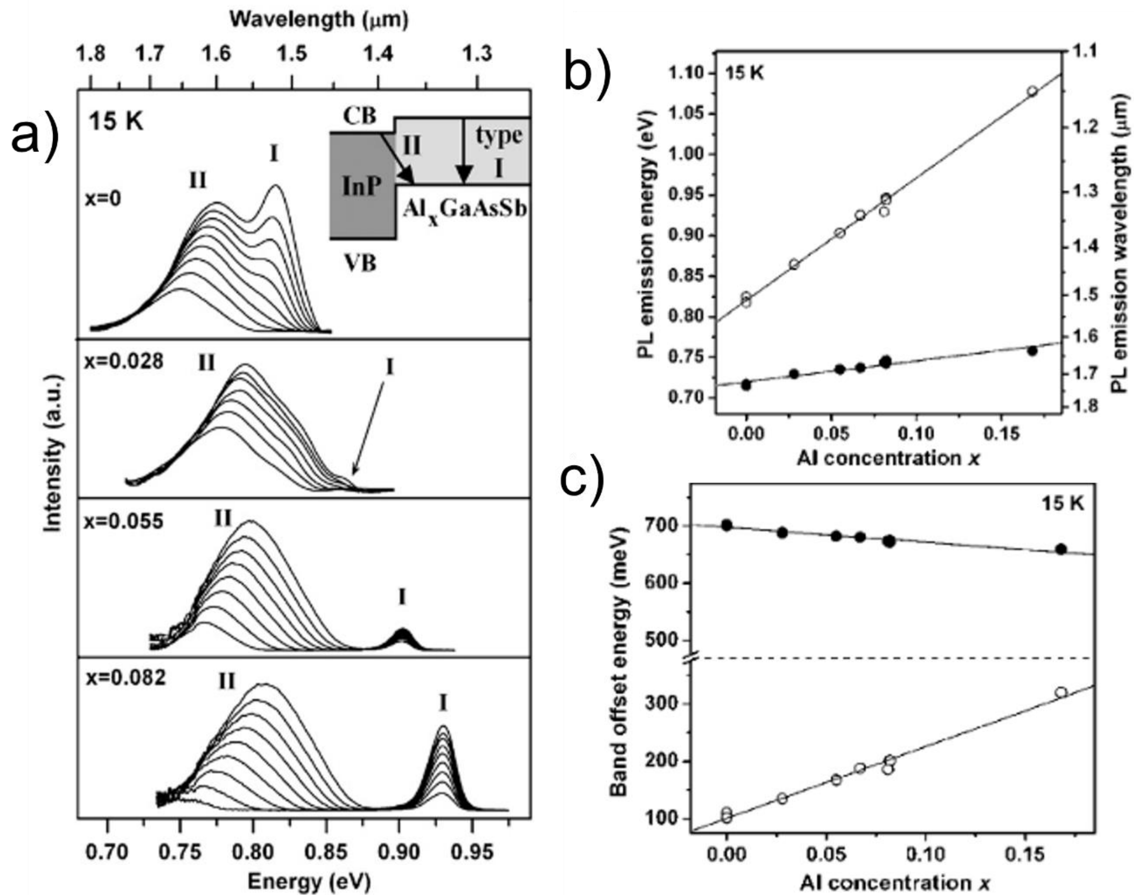

Figure 8- a) The PL peaks from the emission of photons across the AlGaAsSb band gap (type I) and emission from the conduction band of InP to the valance band of AlGaAsSb (Type II) for different amounts of Al incorporation. b) The varying PL emission of type I and II as the Al concentration varied from 0 to ~17%. c) The VBO (black dots) and CBO (white dots) for the range of Al incorporation calculated by subtracting the type II emission from the band gap of InP and AlGaAsSb respectively. Figures from [35].

For the GaAsSb/InGaAs and GaAsSb/InP heterojunctions Hu used a similar technique to determine the CBOs. The structure investigated was InP/InGaAs/GaAsSb and the type II PL emission was measured as the middle InGaAs layer was alternated from a thickness of 1 to 1000 Å. When the InGaAs layer was at its thickest the type II PL emission plateaued at a minimum

value, indicating that the emission was exclusively from recombination of electrons from the CBM of InGaAs to the VBM of GaAsSb. Subtracting this emission value from the bandgap of GaAsSb was used to find the CBO between the InGaAs/GaAsSb interface. When the InGaAs layer's thickness was reduced to a minimum, less than an angstrom, the type II PL emission plateaued at a maximum value. This indicated that the GaAsSb layer was no longer influencing the emission and the signal was exclusively from electrons relaxing from the CBM

Another technique used by Baur found that trace iron impurities in GaN and AlN create a clear characteristic infrared PL band in the materials' PL spectra.[33] They used this information to find the VBO of the heterojunction formed by AlN/GaN based on the excitation thresholds. It was observed that PL emission occurred from the GaN material at an excitation energy of 2.5 eV while the threshold was 3.0 eV for AlN. The difference in the excitation thresholds was the VBO, with GaN's VBM being 0.5 eV above AlN's VBM. The CBO was then calculated by subtracting the VBO and bandgap of GaN from the bandgap of AlN.[33]

A less common technique that has been employed for offset measurements is scanning tunneling spectroscopy (STS) and falls under the electron spectroscopy techniques category. A scanning tunneling microscope (STM) is a tool that can analyze a surface with a resolution that can resolve features as small as 0.1 nm using current from quantum tunneling.[36] A basic STM has a very fine conducting tip that comes to a sharp point. The tip does not physically touch the surface to be measured, instead there is a bias volage applied between the tip and the surface. This voltage encourages electrons to tunnel through the vacuum between the tip and the surface. This electron tunneling creates a tunneling current which is a function of the applied bias voltage, the position of the STM tip and the local density of states (LDOS) of the sample surface.[36], [37] Monitoring the tunneling current generates information about the surface

which is usually displayed in the form of an image that is digitally colored to represent different features.[36] The more refined method of STS involves keeping the tip position fixed while altering the bias voltage to observe changes in the tunneling current, which allows for understanding and even reconstructing the LDOS.[37]

The technique used to determine band offsets with STS involves alternating the distance of the tip of the probe from the sample and sweeping the applied voltage while measuring the tunnel current and conductance with respect to the applied voltage. In figure **9a-c** the raw data from an STS measurement can be seen.

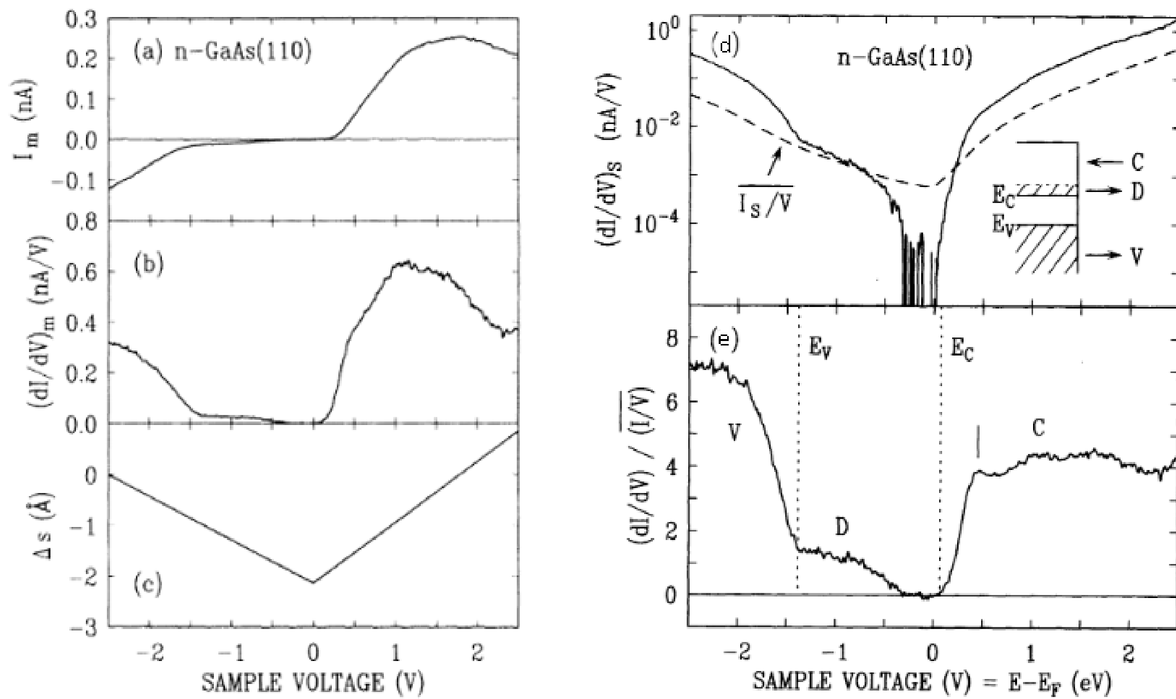

Figure 9 - a) the tunneling current vs applied voltage b) the conductance vs applied voltage c) the probe distance from the surface as applied voltage changes d) the differential conductance with a stationary tip as voltage varies e) the normalized capacitance with respect to the changing voltage. Figures from [38]

Moving the tip with respect to the sample allows for a larger dynamic range in the measurement of the current and conductance, which can be achieved without moving the tip, but the integration time must be increased to achieve suitable dynamic range for the conductance measurement.[38] After the conductance is measured the next step is normalizing the differential conductance dI/dv to the total conductance I/V.[38] In figure 9d the differential conductance with constant tip position is seen, but once normalized with the total conductance in figure 9e distinct regions can be observed. Analyzing the spectra conductance and tunneling current data with respect to the applied voltage allows for identifying the VBM and CBM values with accuracies of ±0.05 eV.[38]

The inherent challenges of this technique has resulted in fewer interfaces being measured compared to other more accessible techniques. STS requires very clean and stable samples and testing typically must be done under ultra-high vacuum.[36]–[38] Most STMs are also built to operate at very low temperatures approaching 0 K and require vibration isolation systems.[36]

Another electron spectroscopy technique that is very commonly used to measure band offsets is x-ray photoelectron spectroscopy (XPS). XPS is a technique that determines the binding energies of electrons ejected from a material based on the measured kinetic energy (KE) of these collected electrons. [39] The techniques name comes from the x-rays that are used to excite electrons from their bonded states. The energy of the x-rays covers a wide spectrum and when an electron in the semiconductor is excited by the appropriate amount of energy it will be ejected. Once ejected from the material a collector will tally the number of ejected electrons as well as measure their KE. From the KE, x-ray excitation energy and work function of the XPS system it is possible to determine the binding energy (BE)of ejected electrons.[39] This provides useful information about what material and core level the electron came from which can be used to identify the composition of a sample. [40]

Beyond material identification, XPS has been used to determine the band offsets of many interfaces. With XPS the band offsets are measured directly rather than being derived from electrical quantities or requiring fitting to complex models.[31] The biggest challenge in the XPS band offset measurement technique is determining the valance band edge (VBE) with an appropriate degree of accuracy. The accuracy ideally should be better than ±0.05 eV when the size of the offsets being measured is considered.[31] The method for determining offsets with XPS starts by measuring a select core level binding energy of the constituent materials that will form the heterojunction. At the same time the VBE for each material must be measured so the difference between the referenced core level energy and the VBE can be determined.[31] Finally, a very shallow interface sample must be measured where the heterojunction is less than a few nanometers bellow the samples surface since XPS can only penetrate about 10 nm into a sample.[40] The same reference binding energies will be measured under the band bending effects of the interface. The separation between these refence binding energies can be interpreted directly as the VBO by using the previously measured core level energies with respect to the VBE.[31]

XPS's high degree of accuracy in directly measuring band offsets has made the technique quite popular. XPS measurements have determined the band offsets of the Ge/GaAs, GaAs/AlAs, InAs/GaAs, Znse/GaAs/Ge, InAs/GaSb and GaSb/AlSb heterostructures with the aforementioned 50 meV accuracy.[31] This technique will be discussed more in section 2.3 as this was one of the methods used in this study to determine the band offsets of GeSn and SiGeSn heterojunctions.

The last offset measurement technique that will be discussed is internal photon emission (IPE) another class of electrical measurement. These measurements plot the quantum yield (Y) vs the photon energy (hv) characteristics of a semiconductor device and distinct energy

thresholds can be observed.[31] As incident light excites the surface of the sample electrons will be energized and move from the VBM of the smaller bandgap material to the CBM of the other material that forms the heterojunction. The threshold excitation energy can be observed in the plot of Y vs $h\upsilon$ as can be seen in figure 10.[41], [42]

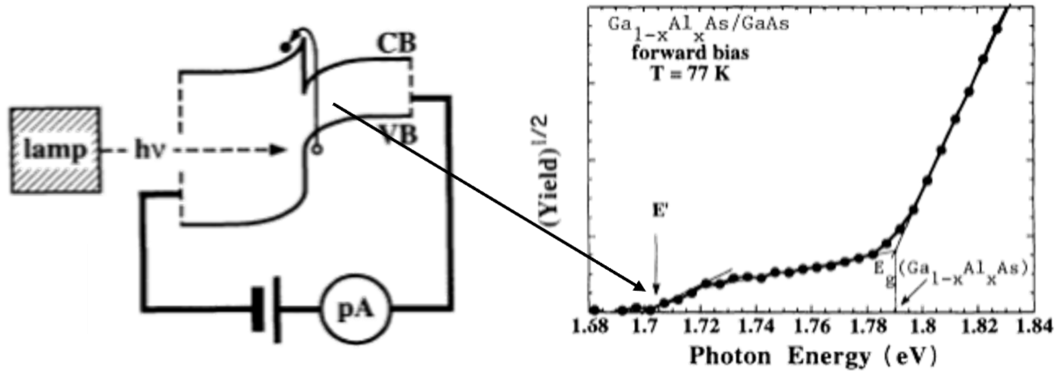

Figure 10 - Schematic of IPE measurement and plot of quantum yield vs photon energy. Distant linear regions show when excitation energy changes the dominant generated photocurrent to change from excitation across the heterojunction to excitation across the bandgap of the larger bandgap material. Figure from [43]

When the photon energy first becomes sufficient to excite electrons from the VBM of one material to the CBM a linear region will be apparent and extrapolating this to the x-axis provides the combined energy of the CBO and bandgap of the smaller bandgap material. Knowing the bandgap of the larger bandgap material allows for subtraction to determine the VBO between the materials. If the bandgap of the smaller bandgap material is also known, then the CBO can also be determined by subtraction.[42] Other techniques have employed free electron lasers (FEL) which can be tuned to only excite the electrons within the CBM. The excitation will directly

measure the CBO by observing the photocurrent generated as electrons overcome the potential barrier in the conduction band and flow across the heterojunction.[44]

IPE measurements have been used to determine the offsets in the interfaces of GaAs/AlGaAs, Si/SiO_2, CdS/CdTe and other semiconductor heterojunctions but is less commonly used than XPS.[31] Some challenges of IPE include the need to fabricate devices on samples for photocurrent measurements, accuracy issues due to fluctuations in dark current and photocurrent, accurate measurement of incident light intensity and correctly extrapolating the quantum yield data to the correct zero yield point. Careful experiment design and data interpretation can minimize the uncertainty to the order of 0.05 – 0.10 eV similar to the accuracy of XPS measurements. With this in mind and having access to device fabrication facilities and appropriate testing apparatuses, IPE was used as the second measurement technique for band offsets in this paper.

2.2 IPE

IPE only differs from external photon emission, the emission of an electron from a solid into vacuum, in that IPE involves the electrons that leave the emitter material being collected in another solid material at the other side of an interface. [45] By observing when these transitions from emitter to collector occur and first overcome the potential barriers that otherwise prevent the flow of photocurrent it is possible to determine band gap values and band offset values of a material. IPE requires additional sample preparation compared to XPS but is not affected by sample strain and does not require additional calculations or characterization save for bandgap measurements.[45]

2.2.1 IPE Theory

The basis of IPE is determining the quantum yield (Y) with respect to the photon energy of an exciting light source that is driving a photoelectric device. Fowler theorized that the quantum yield followed the expression seen in equation 2.

$$(2)\ Y = (hv - \phi)^p$$

Here hv is the photon energy of the exciting light source, ϕ is the barrier height at an interface that must be overcome for charge carriers to move from an emitter material to a collector and p is the spectral dependance that is determined by the functional form of the carrier energy distribution on the surface of the emitter[45]. Quantum yield is not to be confused with quantum efficiency (η) which is the ration of input photon power to output photon power for a device. Instead, the generic definition of Y is the ratio of the number of events to the number of incident photons. A more specific definition for photoelectric devices is the ratio of electrons that escape the emitter material vs the number of incident photons[45]. This can be achieved practically by measuring the photocurrent that flows in a semiconductor device for a given photon energy[42]. From equation 2 ϕ is the minimum energy of the exciting photons that will cause charge carriers to flow across the potential barrier and generate photocurrent. Typically, the exponent p is selected based on the type of material interface is being measured, specifically the emitter material. The original Fowler's law utilizes a p value of 2 for emitters that behave like a metal while a value of 3 is used for semiconductor material emitters[42]. There is still some disagreement about the most suitable exponent to use to properly fit the carrier distribution and many users default to Fowler's original exponent of 2[45].

When the measured photocurrent or a derived quantity such as responsivity (R) which is also a measure of electrical output per optical input is plotted against the excitation photon

energy distinct regions will appear.[42] There will be the so called zero-yield region where the photon energy has yet to exceed the barrier height energy and no photocurrent will flow. This will abruptly transition into a linear region once the threshold is overcome and continue until further charge carriers cannot be excited from the current emitter. Typically, this first region is the result of carrier being excited from the VBM of the smaller bandgap material, across the interface and potential barrier and into the CBM of the larger bandgap material.[42] In this case ϕ is the sum of the bandgap of the small gap material and the CBO. Photocurrent will not flow when only the small gap material's bandgap energy is exceeded because the potential barrier of the CBO still impedes the carriers from crossing to the other end of the device. Linearly extrapolating the zero-yield floor and the linear slope region to where they intersect will determine ϕ[42]. This is the minimum photon energy to cross both the bandgap and the CBO so neither value can be parsed out individually from this lone measurement. Measuring the bandgap of the smaller gap material would allow for determination of the CBO simply by subtracting the band gap energy from ϕ.

Once the photon energy reaches a certain amount there will be another zero-yield region (if the light source can produce high enough energy photons) that is flat or relatively flat as all the carriers in the smaller gap material's VBM are actively being excited and the photocurrent cannot increase further. As the photon energy increases there may be a second linearly increasing region after this second zero-yield region. This slope is a result of carriers being directly excited from the VBM of the larger gap material to the CBM of the large gap material without crossing the interface. This means the photon energy has exceeded bandgap energy of the large gap material. In the same process as the barrier height determination the larger gap material's bandgap can be determined from the intersection of the linear extrapolation of this linear region to the preceding zero-yield region[42].

2.2.2 IPE Equipment Setup

A basic IPE setup involves a photon source, an ammeter capable of measuring small photocurrent, a source of biasing voltage and a photoelectric device that can be probed and biased. Additional features include a method to perform low temperature measurements such as a cryostat as well as a chopper and lock in amplifier to reduce potential noise. Ambient dark current may produce photocurrent before the threshold is reached by photon excitement but chopping the signal at a specific frequency and measuring at this same frequency reduces the effects of dark current in the sample. The light source is of paramount importance as it must be able to produce photons in a range below the barrier height energy to achieve the zero-yield region while also being able to produce photons with energies sufficient to overcome the bandgap of the larger gap material if one intends to measure the VBO. Typically, a tunable laser is used since the step size of photon energies must be small enough to produce clear linear regions and find the precise energy that first exceeds ϕ or the bandgap energy of the large gap material. The measurement does not need to be conducted under vacuum and low temperature measurements is optional to further reduce dark current and thermal effects that may add noise to the measurement. Otherwise the set up mainly hinges on the quality of the device and its ability to be probed under photoexcitation.

2.3 XPS

2.3.1 XPS Theory

At its core XPS is a technique that measures the kinetic energy of an electron, or more accurately the kinetic energy of many electrons that are ejected from a material. This kinetic energy is what is directly measured but is not an intrinsic property of the electrons themselves, the binding energy that held the electron before it was ejected is the desired quantity.[40] Electrons in the various energy bands of their respective atoms are bombarded by x-ray photons. When photons with sufficient energy excite these electrons, they will break free from their bonds and leave the material by overcoming the work function of the spectrometer that performs the counts within the XPS.[40] It can be seen in figure 11 a and b that two generic electrons that are bound in the 1s core level of their respective atom and are excited by an x-ray with sufficient energy to eject the electrons out of the material. In figure 11c a simplified spectra of electron counts vs. KE is displayed, peaks form based on the number of electron counts for a given excitation energy. Typically, the x-axis is a measure binding energy in eV rather than kinetic energy since the binding energy gives insight into the origin of the ejected electrons and thus characterization of the material.[40] In this measurement the excitation x-ray energy (hv), the work function of the spectrometer (φ_s) and the measured KE are all set or measurable or otherwise known quantities. From these known values it is possible to determine the binding energy of the ejected electrons base on equation 3.[40]

$$(3)\quad KE = hv - \varphi_s - BE$$

This is relatively intuitive as the conservation of energy implies that the KE measured will be what remains of the original excitation energy minus the energy required to break free of the original bond and then overcome the vacuum level of the spectrometer.

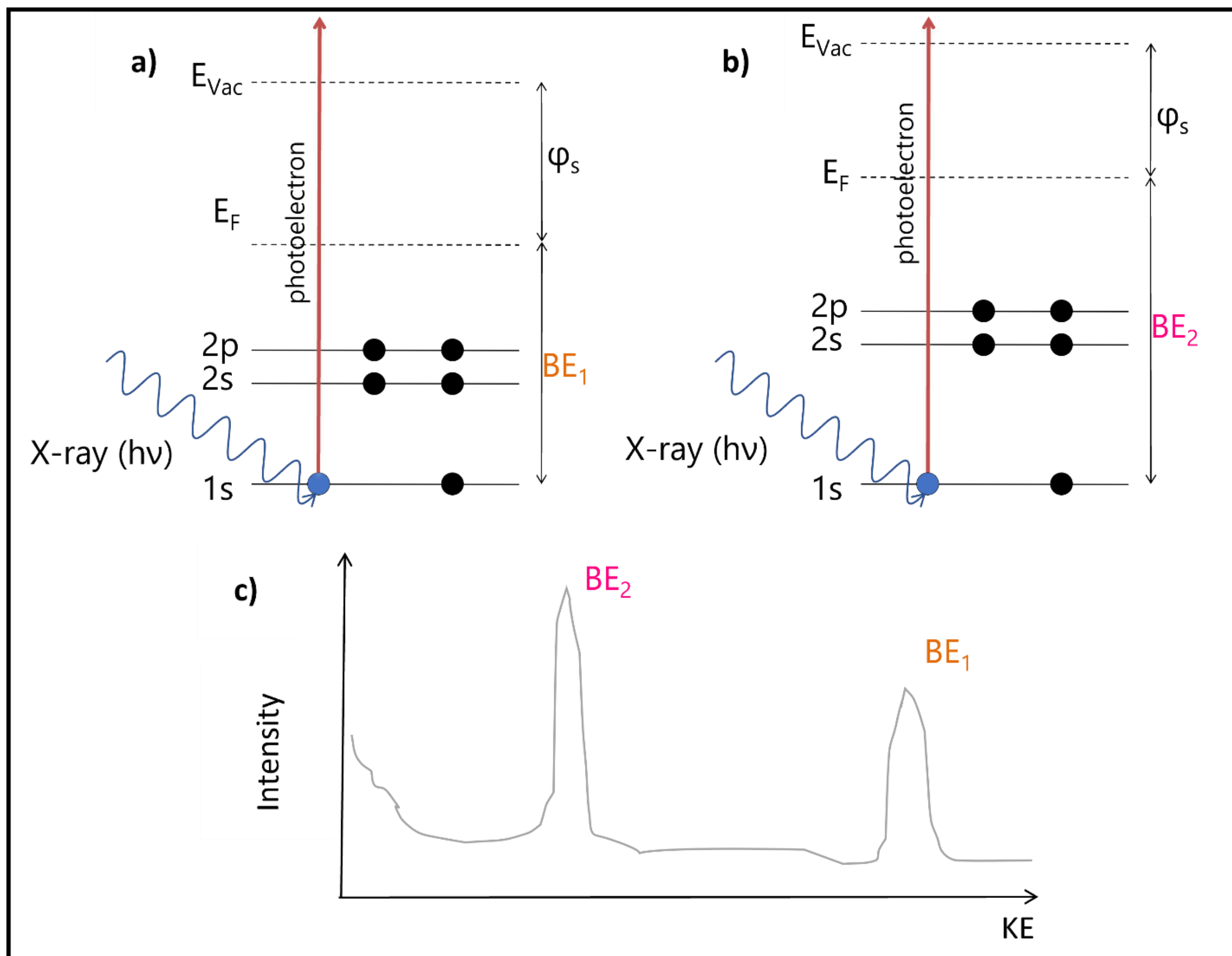

Figure 11- a) and b) show simplified energy diagrams of electrons in core level binding states of generic atoms. c shows the resulting XPS spectra with KE as the x-axis showing that the electron with larger binding energy BE2 has lower KE than BE1.

The technique to determine band offsets using XPS largely came from the efforts of a handful of pioneering researchers in the late 70s by Kraut, Grant, Waldrop and Kowalczyk.

They found that the offsets at a heterojunction could be determined with an accuracy as fine as ± 0.03 eV by measuring specific core level binding energies near the interface under the effects of band bending then measuring the same binding energies further from the interface without the effects of the band bending. [46] XPS is capable of measuring both core level binding energies as well the energy of electrons ejected form the valance band edge (VBE). As figure 12 shows, for most materials just beyond zero binding energy the XPS spectra forms a linear leading edge as counts begin to be registered from ejected electrons. The intersection of the linear extrapolation of this leading edge with the nose floor of the measurement indicates the location of the top of the valance band, the VBM. [47] With this capability one may wonder why core level measurements are necessary. If the top of the valance band can be measured directly one may think that it would be expedient to directly measure the VBM on either side of the interface and thus determine the VBO based on the difference between these values. Unfortunately, this is impossible due to the large band bending that occurs near the interface. Resolving whether the measured VBE was a product of one side of the interface or the other or even influenced by both sides simultaneously is unknowable, rendering the direct measurement of VBM at the interface fruitless.[46]

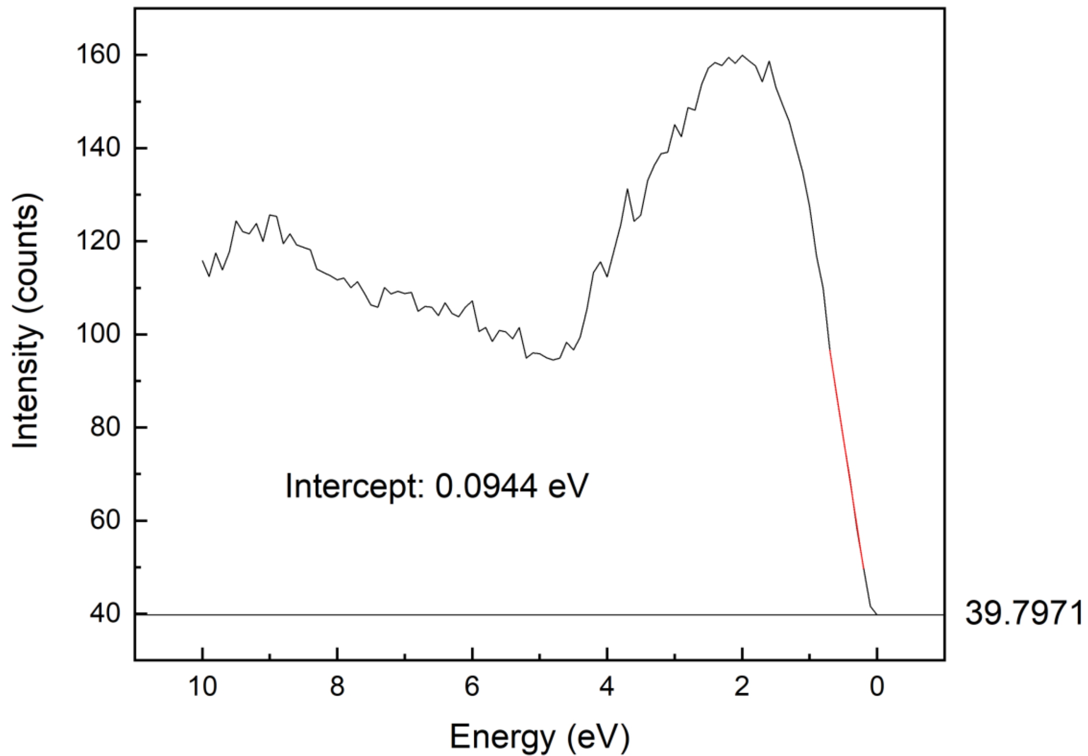

Figure 12- Measurement of the valance band edge of a Ge sample. The red portion represents the fit of the linear leading edge which is extrapolated to the noise floor. The intercept of these lines is the maximum of the valance band.

Yet ingenuity on the part of Kraut et al. allowed for a method to measure the VBE far from the interface then shift the values to account for the band bending. Band bending effects only extend a few nanometers from the actual interface between two materials. In the bulk material the VBE can be measured without influence of the band bending and the measured VBM corresponds to only one side of the interface.[46] Yet for the sake of modeling and understanding the physics that will determine device behavior, the VBM must be known at the interface under the effects of the band bending. Since the VBE cannot be directly measured at the interface Kraut et al. measured the binding energies of electrons from core energy levels in

the bulk material and then near the interface. The core level energies can still be resolved at the interface and will be shifted due to band bending or interface states by the same magnitude as the VBE in the same material.[46] Therefore, the same core level energy can be measured in the bulk material and the difference due to the shifting at the interface can be determined and used to correct the VBM values.

In equation 4 this relationship can be seen more apparently as the difference between the core level energies and VBE energies of the bulk material and the difference in the core level energies at the interface.

$$(4)\ \Delta E_v = (E_{CL}^{Y} - E_v^{Y}) - (E_{CL}^{X} - E_v^{X}) - \Delta E_{CL}$$

Here ΔE_v is the VBO, E_{CL}^{Y} and E_{CL}^{X} are a specific core level binding energy measured in the bulk material from material Y and X respectively which are the two materials that compose the heterojunction. E_v^{Y} and E_v^{X} are the energies at the top of the VBEs in the bulk material from material Y and X respectively. Finally, ΔE_{CL} is equal to $E_{CL}^{Y}(i) - E_{CL}^{X}(i)$, which are the same core level energies as E_{CL}^{Y} and E_{CL}^{X} respectively but measured at the interface. The arrangement of equation 4 is significant. If the quantity $(E_{CL}^{Y}\text{-}E_v^{Y})$ is instead subtracted from $(E_{CL}^{X}\text{-}E_v^{X})$ then ΔE_{CL} must become $E_{CL}^{X}(i) - E_{CL}^{Y}(i)$ in order to reflect the energy alignment being determined.[46] As equation 4 is written the offset is determined with respect to the leading material in the first set of parentheses so the offset from material Y to material X. positive ΔE_v indicates that the VBM of material Y is above that of material X while a negative value indicates the VBM of material Y is below the VBM of material X. This method finds the VBO directly, if the bandgap of both materials can be determined by other methods, then the CBO can also be calculated by subtraction of the bandgap energies and the VBO[46].

This method requires core level measurements to be taken very close to the interface, since the measurement depth of XPS is less than 10 nm this requires a very thin layer to be grown on top of the second material or etching/sputtering to be performed to reduce the thickness of the top layer. The VBE measurement must also be taken with care. Electron counts in this region are much fewer compared to core level binding energies as can be seen by comparing the intensity of figure 11 and figure 12. Kraut et al. developed a more precise method that involves using least squares fit of the instrumentally broadened valance band density of states around the estimated VBM energy. The complexity of this measurement has resulted in many characterizations settling for the linear extrapolation which many papers have used to report offset values with accuracies on the order of hundredths of electron volts.[48]–[51]

2.3.2 XPS Equipment Setup

A typical XPS instrument consists of four main components. First is an excitation source which can either be an X-ray source which forms the main beam used to eject electrons from a sample. Second is an electron detector and analyzer system which can measure the ejected electrons accurately. Third is a vacuum system that contains all these components and the sample with a sufficiently strong vacuum to prevent ejected electrons from colliding with undesired ambient particles. Finally, a data system which interprets the results has become standard for fitting and analysis.[39]

Ultra-high vacuum is considered to be pressure ranges from $10^{-8} - 10^{-10}$ mbar[3] and it has become a staple of XPS analysis that measurements be performed within these pressure regimes for low enough noise levels for accurate measurements.[39] Moreover, in a vacuum less than 10^{-6} mbar[3] it is possible for a gas layer to adsorb to the surface of a sample in the span of a single

second. This is much faster than the time it takes to acquire a spectrum collection via XPS thus perpetual phantom elements may appear in the spectrum in poor vacuum conditions.[39] Other considerations are the pumps used to create the vacuum and shielding against the earth's magnetic field. Ion and turbopumps are common choices for XPS systems while diffusion pumps have largely been phased out. A sublimation pump is often used to supplement the main pump to reach the desired vacuum level.[39] Besides the vacuum level, the trajectory of electrons within and XPS chamber are strongly affected by the earth's magnetic field if they are not shielded in some way. This can be achieved by having the whole chamber made out of a material, such as Mu-metal, that will screen out the magnetic effects or by sleeving within the machine or an external surrounding structure.[39]

The X-ray source of an XPS is typically a twin anode source. In general x-rays are generated by bombarding a anode source material with electrons that are emitted from a thermal source such as a tungsten filament.[39] The anode material determines the energy of the x-rays generated and must generate high enough photon energy to excite all by the lightest elements of the periodic table. A thin x-ray line width that won't broaden the resulting spectrum is also desired. These characteristics make aluminum (Al) and Magnesium (Mg) the most popular choices for anode materials.[39] The configuration typically includes one electron gun that can selectively bombard either the Al anode for AlKα photons with energy 1486.6 eV or the Mg anode for MgKα photons with energy 1253.6 eV.[39] Having two anode materials can be useful to distinguish XPS peaks from Auger peaks which are caused when electrons are ejected from an atom to maintain energy conservation when higher energy electrons fall to fill vacancies in lower energy levels an atom. These Auger peaks don't provide core level binding energy information that XPS analyses, but the peaks can overlap with the core level peaks making distinguishing them more difficult. If the x-ray energy

changes by switching anode materials all of the core level binding energy peaks will shift while the Auger peaks will remain in the same place since they are not directly excited by the x-ray source. [39]

Commercial XPS systems can utilize two types of electron energy analyzers to determine the binding energies of ejected electrons. There is the cylindrical mirror analyzer (CMA) and the hemispherical sector analyzer (HAS) demanding on the type of measurements the user will be making, although a typical XPS system will only have one analyzer. A basic schematic of both analyzers can be seen in figure 13 with the CMA on the left and the HAS on the right, it is apparent that they owe their name sakes to their geometry.

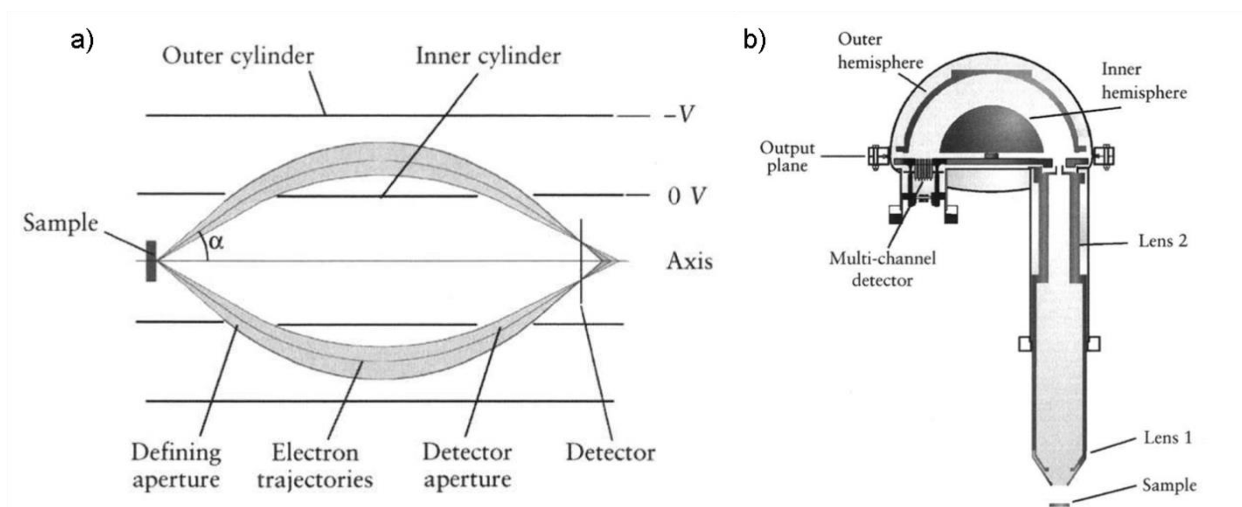

Figure 13 - a) is a cylindrical mirror analyzer showing the trajectory of electrons from sample to detector. b) is a hemispherical sector analyzer with attached lenses that retard electrons before they reach the detector .Figure from[39].

The cylindrical detector has an interior and exterior concentric cylinder held at different electrical potentials. The inner cylinder is kept at earth potential while the exterior cylinder is given a negative potential. Electrons ejected from the sample will pass through the apertures of the inner cylinder if they posses the desired energy, controlling the applied voltage on the outer cylinder alters electron trajectories sorting them based on their energy.[39] Those that pass

through both apertures make it to the detector to be counted and contribute to the spectra. Typically the CMA is used for Auger electron spectroscopy rather than for XPS due to the resolution being lower than what is necessary to discern chemical state information from electron KE.[39]

The HAS is the standard for XPS measurements and uses concentric hemispherical electrodes with varying electrical potential to guide collected electrons to the detector. Electrons with insufficient or excessive energy will deviate from the path and not reach the detector. The voltages of the electrodes will adjust electron trajectories if they're energy is not too far from the potential equidistant between the two electrodes.[39] To increase the likelihood of electrons having the proper energy by the time they reach the detector most systems will have a lens or series of lenes before the hemisphere chamber. These lenses retard the energy of ejected electrons to a level that can be properly detected by the HAS.[39]

The instrument that was used for the measurements in this paper was a PHI Versaprobe 5000 X-ray photoelectron spectrometer which uses a Al anode as its primary beam source. The lowest vacuum pressure main chamber reached was 1E-7 pascals, while during operation the pressure was in the 1E-6 pascal regime. The system is equipped with a electron flood gun, a neutralizer that operated during scans to reduce the likelihood of unequal charge accumulation on the surface of the samples which would shift binding energy peaks. MultiPak was the software suit used to fit and analyze the spectra as it was measured.

Chapter 3 XPS Heterostructure Measurements

3.1 Sample Selection and Preparation

The PHI Versaprobe 5000 X-ray photoelectron spectrometer does not feature the option to transfer samples directly from a growth chamber or from vacuum into the chamber. Instead, samples are introduced from atmosphere to an introduction chamber that is then sealed and pumped down sufficiently so sample could be transferred to the main chamber. To fit the stages used in the XPS samples were cleaved to 2 mm x 2 mm squares whose surfaces were cleaned by isopropanol alcohol (IPA) and microfiber tissues. Samples were mounted on stages via small double stick tape pads and then transferred after sufficient pump down, typically a half-hour for Ge and GeSn samples.

An early discovery was that samples containing Ge oxidize incredibly quickly in atmosphere. While GeO_2 bonds can be broken simply by washing with hot water, the GeO bonds were more resilient. Moreover, samples could not be introduced into the introduction chamber while wet due to potential damage to the system. The formation of surface oxide was so quick that the time required to dry, mount and place the sample into vacuum was sufficient for most of the surface oxide to reform. It was important to remove this surface oxide because the energy of the GeO bonds overlapped with the energy of the Ge 3d core level energies that were used as part of the offset determination. This broadened and shifted the peaks making accurate determination of the binding energies difficult. Two methods were used to remove surface oxide, chemical wet etching with hydrogen surface passivation and sputtering.

Chemical wet etching uses a chemical process that typically uses acids and oxidizers to remove material from the surface of a sample at a calibrated etch rate. To remove the surface

oxide a “piranha etch” was used which targets oxides but does not break bonds between Si and while it does etch Ge related materials the rate is much slower than the oxide removal. The etch is composed of a 1:1 mixture of sulfuric acid (H_2SO_4) and hydrogen peroxide (H_2O_2) which the sample is submerged in for approximately 5 minutes. This step of the etch removed the oxide from the sample surface, but hazards associated with the chemicals prevented this etch to be performed in the same laboratory that housed the XPS system. Therefore, a method to keep the oxide from reforming on the sample surface while it was transferred to the vacuum chamber was required. To stop the formation of oxide during this transfer a layer of hydrogen was formed on top of the sample through hydrogen passivation. As soon as the 5-minute etch was complete the samples were put into a separate beaker with a 1:10 ration of hydrofluoric acid HF and DI water for 1 minute. This process forms a hydrogen layer without any dangling bonds for oxides to attach to, preventing oxidization of the surface. This hydrogen layer is relatively volatile and will evaporate off the sample surface in roughly a half hour, which gives sufficient time to transfer into the vacuum chamber. This technique was useful for the samples with thick layers to be measured for the core levels without the effects of the interface but was less applicable to the thin layer samples. The piranha etch does attack Ge surfaces to some extent as this process was intended to clean Si wafers as growth substrates, so it was not made with Ge in mind. For thick samples this is not an issue since XPS only analyzes the first 10 nm and the layers are homogenous throughout. For the thin interface samples there was a risk of etching away the top layer completely since it had to be ~5 nm or less for the interface to be analyzed.

In both cases where chemical etching could and could not be used, fine surface cleaning was performed inside the XPS chamber via sputtering. Sputtering is a process of bombarding a surface with inert ions to knock apart the bonds at the surface and dig into the material. It has been shown that high energy sputtering can alter the chemical states of semiconductor surfaces

so only low energy sputter was used to clear sample surfaces. At low power sputtering could take as long as 3-munutes to remove surface oxidization from samples that had not been wet etched. Sputtering also fills the chamber with ambient particles which reduces the overall vacuum quality and requires additional pump down time until samples can then be measured. Because of these challenges, whenever possible chemical etching was used to reduce surface oxide, other wise samples were washed and dried quickly with nitrogen gas to remove surface oxide and reduce the reliance on sputtering.

Etching was also used to bring the interface samples to the appropriate thickness where the heterojunction could be probed by the x-rays. Growing 5 nm layers can be challenging so existing samples with top layers exceeding this thickness were selected and then wet etched down to the appropriate thickness. Rather than the piranha etch, a more refined etch which consisted of a mixture of 1:1:20 hydrochloric acid (HCL), H_2O_2 and DI water was used. This mixture is effective at etching at a constant rate in Ge and GeSn and when the solution is cooled to nearly zero centigrade the etch rate is ~20 nm per minute. This relatively slow etch rate allowed for precise top layer thicknesses to be achieved by etching then immediately quenching in DI water to end the etch. Thicknesses before and after the etching were confirmed by ellipsometry measurements.

Samples were selected first for calibration of the technique. The XPS measurement of GeSna and SiGeSn are novel measurements without literature to reference for comparison. To ensure the technique and equipment was functioning as intended calibration on similar materials that can be referenced in literature were measured first. Namely Ge on Si and Ge on GaAs samples were used to build confidence in the technique. These samples were primary chosen based on material quality and thin top layer thickness to reduce the amount of etching and sputtering required for sample prep. The GeSn/Ge sample was chosen for its Sn content (10%) to

exceed the threshold for direct bandgap, while remaining high quality since higher Sn incorporation samples are more difficult to grow. Complications with the XPS measurements prevented additional GeSn samples from being considered.

3.2 Calibration Measurements

In order to build confidence in the technique calibration measurements on the band offset between Ge and various substrates that that were already fairly well documented were performed to ensure the reliability of the measurements. These were primarily Ge/Si samples with a few Ge/GaAs measurements. The Ge samples consisted of 0049-UAF, 0050-UAF and 0255-UAF all of which were Ge grown on Si (001) substrates by CVD growth. The Ge/GaAs sample, GA01 was a MBE grown Al/Ge/GaAs(100) sample and the Al layer was removed through chemical etching. Three separate specimens were prepared for each sample group, 2 mm by 2 mm square sections prepared by cleaving. One specimen from each group kept the top layer thickness unchanged to measure the Ge core level energies and VBM without the influence of the interface. The second specimen in each set was the interface sample, this required chemical etching to reduce the top layer thickness to only a few nm so the interface could be analyzed by the relatively low power x-rays of the XPS. The final specimen in each set was the Si substrate after completely etching away the Ge top layer in order to measure the core level energies and VBM of Si without interface effects.

Samples were cleaned with chemical etching and preserved with hydrogen passivation, when possible, interface samples had to rely solely on sputtering to remove surface oxidization due to how thin the top layer was. For all samples the Ge 3d core level was selected to be measured since its binding energy is relatively far from the Si 2p and 2s binding energies that

were used for the Si material and the 3d electrons have higher KE than Ge 2p electrons. The NIST database reports Ge 3d binding energies in the range of 28.60 – 29.70 eV. For Si 2p and 2s the NIST database reports values from 98.40-99.67 eV and 150.50-150.70 eV respectively. In the Ge/GaAs samples the Ge 3d binding energies were still used for Ge while the Ga 3d and As 3d binding energies were used. According to the NIST data base the Ga 3d and As 3d binding energies are 18.73-19.70 eV and 40.70-41.60 eV respectively. Once again, these core levels were chosen for having relatively high KE electrons for clearer peaks in the spectra. As the NIST data shows there can be variation in measured core level energies, some of which is quite large. This can be from any number of factors ranging from sample preparation to surface charging or even sample material quality. Therefore, most papers measuring band offsets do not report individual binding energies, instead they report the differences from equation 4. This removes the potential error from the relative shifting of peaks as all peaks will be shifted by the same amount if there is surface charging or other effects.

Measured values were therefore compared to literature based on the core level to core level and core level to VBM values. Table 2 shows the determined energy differences for the Ge/GaAs sample.

Table 2- Ge/GaAs XPS values

Interface	$E_{As3d}^{GaAs} - E_{VBM}^{GaAs}$	$E_{Ga3d}^{GaAs} - E_{VBM}^{GaAs}$	$E_{Ge3d}^{Ge} - E_{VBM}^{Ge}$	$E_{Ga3d}^{GaAs} - E_{Ge3d}^{Ge}$	$E_{As3d}^{GaAs} - E_{Ge3d}^{Ge}$
Ge/GaAs (Oxidized)	40.77	18.75	28.9	-10.55	11.47
Ge/GaAs	41.12	19.18	-	-10.11	11.83

The referenced literature found values for E_{As3d}^{GaAs}-E_{VBM}^{GaAs} to be 40.79 and 40.34 eV, the E_{Ga3d}^{GaAs}-E_{VBM}^{GaAs} seperation to be 18.80 eV, the E_{Ge3d}^{Ge}-E_{VBM}^{Ge} seperation as 29.57 and 29.52 eV, the seperation between E_{As3d}^{GaAs}-E_{Ge3d}^{Ge} as 11.78 and 11.05 and the E_{Ge3d}^{Ge}-E_{Ga3d}^{GaAs} seperation to be – 10.21 eV [52], [53]. In most of these measurments both references are in fairly close agreement sae for the E_{As3d}^{GaAs}-E_{Ge3d}^{Ge} seperation in which the measurments vary by over 0.7 eV. My own measurments are strangly in better agreement for the core level to VBM seperation for the oxidized values, being within ±0.05 eV for the Ga 3d and As 3d to VBM seperations. For the Ge 3d to VBM seperation the agreement lesser, with more than a 0.6 eV disagreement with the referenced values. The unoxidized core level seperation between As 3d and Ge3d is in fairly good agreement with one of the references, but there is a large disparity between the references for this seperation. Finally the Ge 3d-Ga 3d seperation only varies by 0.1 eV from the reference for the unoxidized sample. This result is interesting as it suggest the references may have had some oxidation on their samples still since the As 3d and Ga 3d to VBM values are in such close alignment, at the same time this only seems to be the case for seperation between the core level to VBM values. The unoxidized sample values for core level seperations are in better agreement than the oxidized sample values which may suggest that sputtering had some impact on the VBM of the

unoxidized sample thus causing some disparity due to surface damge. The final VBO calculated using the oxidized values comes to -0.4 eV using the Ga 3d core level and 0.4 eV using the As 3d core level. The sign difference is a result of how the energy levels are refererenced to one another, in both cases the GaAs VBM is above (lower eV) the Ge VBM by 0.4 eV. The references find an offset of 0.56 eV and 0.42 eV [52], [53]. It is worth noting the 0.56 eV offset is from a Ge/GaAs (110) interface while the 0.42 eV offset is from a Ge/GaAs (001) interface and crystal orientation plays a major role in forming heterojunction band structure.

Similar to the Ge/GaAs values the determined core level to core level and core level to VBM seperation values for the Ge/Si interface can be seen in table 3.

Table 3 - Ge/Si as well as pure Ge substrate XPS core level and core level to VBM separation values

Interface	$E^{Si}_{Si2p} - E^{Si}_{VBM}$	$E^{Si}_{Si2s} - E^{Si}_{VBM}$	$E^{Ge}_{Ge3d} - E^{Ge}_{VBM}$	$E^{Si}_{Si2p} - E^{Ge}_{Ge3d}$	$E^{Si}_{Si2s} - E^{Ge}_{Ge3d}$
Ge/Si (Oxidized)	99.05	150.24	30.57	68.44	119.63
Ge/Si	98.99	150.23	29.30	70.06	121.36
Ge/Si	-	-	29.55	70.08	-
Ge/Si	-	-	29.43	70.03	-
Ge/Si	-	-	29.35	-	-
Ge Ref	-	-	29.58	-	-
Ge Ref	-	-	29.51	-	-

Here a large emphasis was placed on the Ge 3d to VBM measurments as there was large variation between measurments while the Si core level to VBM values were relatively consitant even in the prescence of surface oxide and the Si core level to Ge core level values were consistent when the surface oxide was removed. This lead to the conclusion that the Ge VBM determination was leading to the disperity. Refering back to figure 12 the fitting of the VBE involves a linear extrapolation that is responsible for the largest portion of the potential error in the measurment. While the linear regions were fairly distinct, the number of counts near the VBE are much lower than for core level binding energies, which could result in spectra in this region that is a less than accurate representation of the VBM. Additionally the possiblity that sputtering surface damage due to sputtering was changing the VBE could not be ruled out since all samples had some level of oxidization and low energy sputter was used to remove this oxide.

Reference literature primarily used the Si 2p core levels and Ge 3d core levles and found the E^{Si}_{Si2p}-E^{Si}_{VBM} separation to be 99.01 and 98.95 eV, the E^{Ge}_{Ge3d}-E^{Ge}_{VBM} separation as 29.57 and 29.41 eV and the E^{Si}_{Si2p}-E^{Ge}_{Ge3d} separation to be 70.12 and 70.09 eV[54], [55]. Here it can be seen that the majority of my determined energy separations are in good agreement with the referenced literature. The E^{Si}_{Si2p}-E^{Si}_{VBM} only deviates by ~0.04 eV and the E^{Si}_{Si2p}-E^{Ge}_{Ge3d} only differs by 0.09 eV at most. The disparity comes in to play with the E^{Ge}_{Ge3d}-E^{Ge}_{VBM} separation. Between the two references there is already a sizable disparity of 0.16 eV for this separation. While many of my own values fall into this range there are outliers in both directions. Averaging the six non-oxidized values for the Ge 3d to VBM separation yields and average separation of 29.45 eV and averaging the values of the core level separation between Si 2p and Ge 3d yields and average of 70.05 eV. Using these values with the Si core level to VBM separation results in a VBO of -0.51 compared to literature values 0.74 and 0.83 eV. The large disparity between obtained offset and

literature stems from additional steps taken in the calculations performed in the literature. In strained samples there is the possibility that the valance band splits and resolving the maximum of this valance band requires theoretical predictions or additional x-ray diffraction measurements.[54], [55] The additional theoretical calculations and diffraction measurements can be performed as future work to better understand this strain effect.

3.3 GeSn Results and Discussion

With the potential sources of error in mind only a single measurement was performed on the GeSn/Ge interface which lacks any empirical literature to reference the determined value against. ASM-0016 was used to attempt to determine the VBO between a GeSn layer with 10% Sn and the Ge buffer it was grown on. The Sn 3d 3/2 and Sn 3d 5/2 core level energies were used for the GeSn core level while Ge 3d was used for the Ge buffer core level energy. From figures 14 and 15 it can be seen that the effect of Sn on shifting the core level energy peaks is relatively small. The lower left graph shows the Ge 3d core level peaks for both thick GeSn and thick Ge. Only the core level from the thick Ge layer is used in the determination calculation, but this shows the different binding energy in the GeSn environment compared to pure Ge buffer. Similarly, there are only small shifts in the Sn core levels in the thick material and the interface material, the Sn 3d5/2 core level energy actually does not shift at all. From figure 15 it can be seen that the VBE data has a distinct linear region for both the GeSn layer and the Ge layer, but the spectra is choppy. Like all the spectra ~3 hours of collection was used to collect this data, but the counts were still particularly low. Additional time would allow for a smoother curve and may improve the quality of the linear extrapolation, but operational time on the equipment is limited.

The regions overlap significantly in the linear portion and the best fit results in a shared VBM of -0.59 eV in the thick layers.

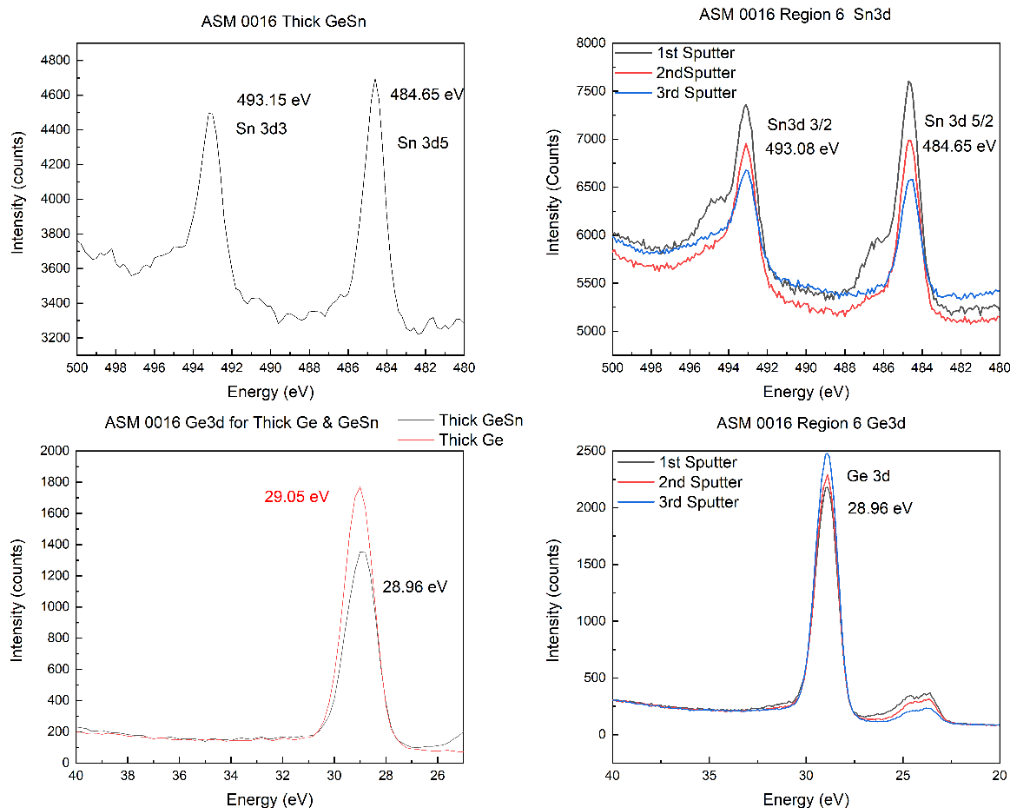

Figure 14 - Core level XPS spectra for ASM-0016. Upper left is Sn core level energies in the thick GeSn layer and bottom left is Ge 3d core level energy in thick Ge and in thick GeSn for comparison to show the shift in core level energy. Upper right is the Sn core levels in the interface sample and lower right is the Ge 3d core level in the interface sample both at different stages of sputtering.

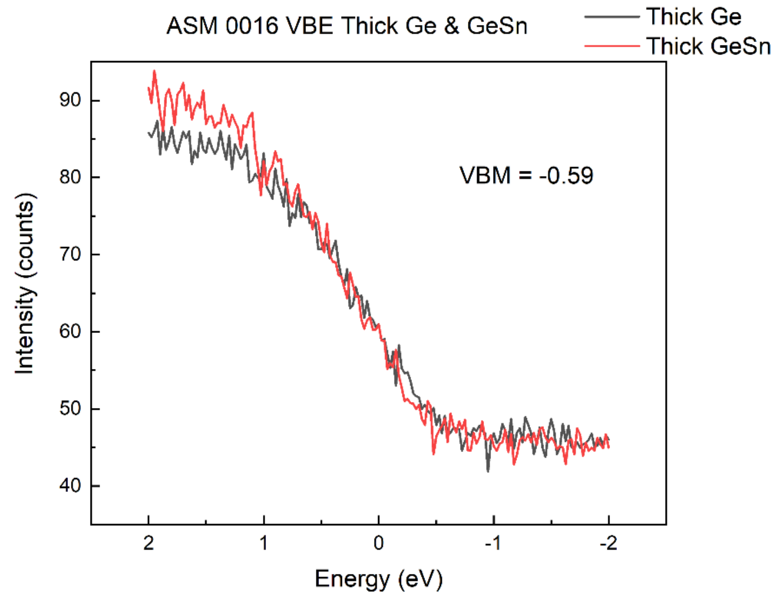

Figure 15 – VBE XPS spectra for thick Ge and GeSn layers of ASM-0016

The calculated energy separation results of the XPS measurements can be seen in table 4.

Table 4 - XPS determined core level and VBE separation energies for ASM-0016

Interface	$E_{Sn3d3/2}^{Gesn} - E_{VBM}^{Gesn}$	$E_{Sn3d5/2}^{GeSn} - E_{VBM}^{GeSn}$	$E_{Ge3d}^{Ge} - E_{VBM}^{Ge}$	$E_{Sn3d3/2}^{GeSn} - E_{Ge3d}^{Ge}$	$E_{Sn3d5/2}^{GaSn} - E_{Ge3d}^{Ge}$
GeSn/Ge	493.74	485.24	29.64	464.12	455.69

Using the Sn 3d3/2 core level energies a VBO of -0.02 eV is determined while using the Sn 3d5/2 core level results in a VBO of -0.09 eV. Since the same VBE values were used in conjunction with each Sn core level the error must arise from the determination of the Sn 3d3/2 and 3d5/2 energies since the resulting VBO should be the same regardless of referenced core level energy. Given that the error associated with this measurement is within ±0.1 eV the

disparity is not incredibly surprising. Based on the XPS results it is found that the VBM of the Ge buffer is slightly above the VBM of GeSn and there is a small VBO of only a few hundredths of an electron volt. The CBO cannot be determined directly from XPS data but could be determined if the band gaps of both materials were determined by optical measurements.

Chapter 4 IPE Heterostructure Measurements

4.1 Sample Design and Considerations

As discussed in section 2.2.1 and 2.2.2 IPE measures the threshold energy between the VBM of the small gap material and the CBM of the large gap material. In order to facilitate this measurement a proper sample and fabricated device are necessary. The threshold ϕ and bandgap of the large gap material are both determined by linear extrapolation of the Y vs. hv data for the device, but interpretation of this data can be very challenging depending on the interface in question. If the band gap of both materials is very similar and the band offsets small there is the possibility that a clear linear region of the photocurrent flowing from the smaller VBM to the larger CBM can't be resolved. The transition from carriers being excited across the interface to carriers being excited directly across the large bandgap material my be so sudden that the regions overlap. In this case neither ϕ nor the large gap material's band gap will be able to be determined. For this reason, the semiconductor material interface had to be designed with a large disparity between the large and small gap material's bandgaps. Fortunately, Si's bandgap of 1.12 eV is much larger than Ge's 0.661 eV bandgap and makes the bandgap of SiGeSn much larger than that of GeSn. Additionally, a larger amount of Sn was incorporated into the GeSn layer which further reduces the bandgap of the GeSn layer. The sample structure of FDY-0106 revealed by secondary-ion mass spectrometry (SIMS) is shown in figure 16.

SiGeSn 71.5 nm 2.4%Si, 8.4% Sn
GeSn QW 39.1 nm 11.8% Sn
SiGeSn Cap 73.8 nm 2.2%Si, 8.4% Sn
GeSn Buffer 850 nm 6~9 % Sn
Ge Buffer 560 nm
Substrate

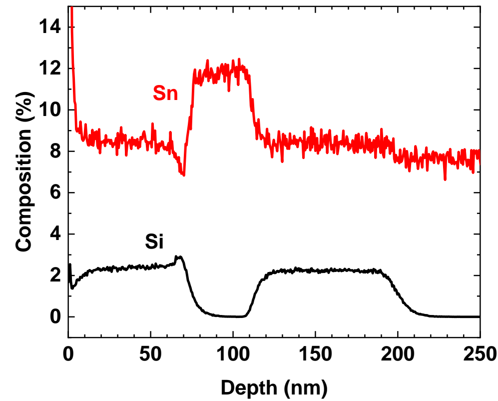

Figure 16 - Structure of sample FDY-0106 as revealed by SIMs. The red and green layers represent the two sides of the measured heterojunction.

This is a single quantum well (QW) sample with a smaller bandgap GeSn layer confined between two SiGeSn cap layers. The lower cap layer is grown on a 850 nm GeSn buffer which exceeds the critical thickness of 700 nm to ensure the top layers and interfaces will be strain and defect free. The Prescence of defects at or near the SiGeSn/GeSn interface could introduce electronic levels into the bandgap of either material which would potentially allow a path for photocurrent to flow at a lower photon energy than ϕ or the bandgap of SiGeSn. This would make the quantum yield vs hv data unusable for finding the band offsets, since it would be unclear what energy gaps were contributing to the minimum photon energy threshold for photocurrent.

4.2 Device Fabrication

The IPE device was fabricated on sample FDY-0106 whose structure can be seen in the previous section. The device is a square photodiode made through typical wet etching and

photolithography and metal deposition processes[56]. First the sample was cleaned with acetone and IPA to ensure the surface was clear of any contamination. Next AZ4110 photoresist is spin coated on the surface of the sample and spun at 4000 rpm with a target resist thickness of 1.7 um. Afterwards the accumulation at the sample edges is removed abrasively and a 50 second soft bake on a hotplate at 110℃ dries the photoresist.

Following the soft bake, the first alignment was performed on the photolithography aligner. The first photodiode square mask was put in place, aligned and the sample was exposed at an energy of 4.52 mJ/cm^2 for 11 seconds. Afterward the sample was introduced to a solution of AZ300 MIF developer for 45 seconds and checked under a microscope to confirm that the photoresist was sufficiently developed. This was followed by a hard bake on a hot plate at 130˚C for 2 minutes and the photoresist was then removed through chemical etching with a 1:1:10 mixture of H_2O_2, HCL and water. A SiO_2 layer 4000 Å thick was deposited through E-beam evaporation and the process proceeds to the second photolithography alignment. The sample was prepared, and spin coated as previously described except AZ5214 resist was used and spin coated at 3000 rpm with a target thickness of 1.8 um.

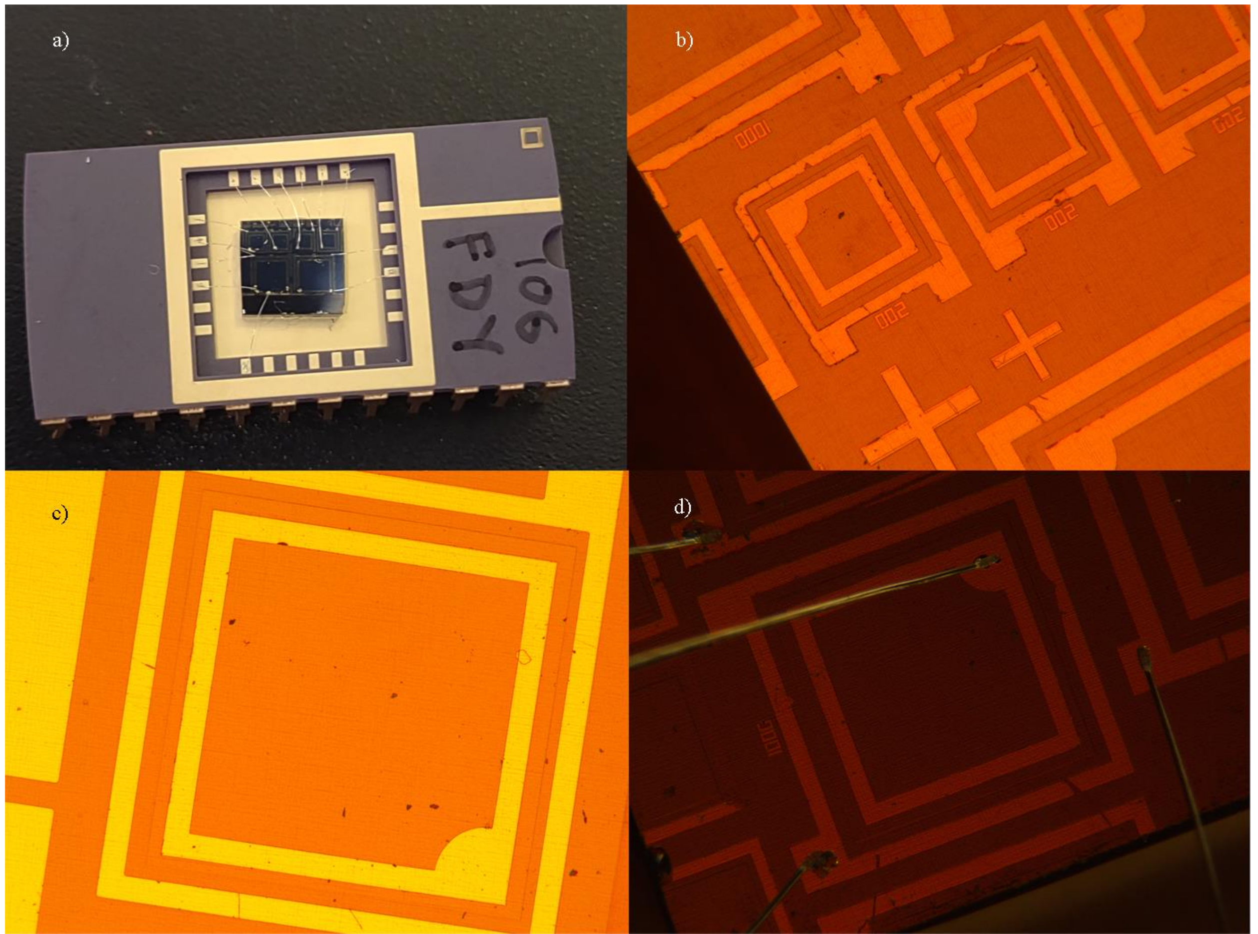

Figure 17- FDY 0106 post fabrication. a) shows the chip wire bonded to the chip holder used to interface with the cryostat used for the photocurrent measurements. b) shows some of the lower quality devices fabricated on the sample. c) shows one of the high-quality devices. d) is a image of the wire bonded device used for the IPE measurements.

The second mask alignment was performed, and the sample was first exposed for 6 seconds with the mask and then a flood exposure for 1 minute without the mask present. The sample was placed in the AZ300 MIF developer for ~30 seconds, dried and then placed in a Descum for 3 minutes for cleaning. The oxide was then removed, and the final alignment was performed with the same steps as the second alignment except using the third mask; exposure and flood time are the same. The sample was then placed in developer, dried and placed in the

Descum for cleaning. Finally metal deposition of chromium (Cr) and gold (Au) 100 angstroms and 4000 angstroms respectively formed the contacts and lift off was performed to remove the excess metal. Wire bonding was used to connect a number of the devices to a test structure that fit into the cryostat of the IPE testing setup. In figure 17 the fabricated chip can be seen on the device holder and microscope images were taken of individual devices. There was some variation in device quality where over etching of some devices made them unsuitable for wire bonding and operation while others were high quality. This may have been a result of unequal light exposure in the aligner which made the resist more and less developed.

4.3 Construction of Unique IPE Testing Setup

The testing apparatus used for the IPE measurements fits the described set up outlined in section 2.2.2 with a few additional features. The photon source in this set up was a tunable 3 μm laser capable of wavelengths from 1897 to 3005 nm and power up to 4.8 W. The laser was guided through the optical path to the cryostat that housed the sample by lining up the path with that of a 532nm green laser. The laser path includes a 50:50 beam splitter that guided the beam to the sample as well as a flippable power meter that was placed at an equal distance to ensure the measured power was equivalent to the power reaching the sample. The laser stepper motors could be controlled through computer software to adjust the output wavelength of the beam. Yet the actual wavelength needed to be known accurately so the laser path also guided the beam into an FTIR which used a commercial detector to determine the laser wavelength. To protect the detector used with the FTIR an adjustable neutral density filter was used to reduce the power of the beam to safe levels.

A schematic diagram of the IPE path can be seen in figure 18. A chopper was used along with a lock in amplifier to reduce measured responses that were not a result of excitation signal. The cryostat was filled with liquid nitrogen and controlled to reach a series of test temperatures ranging from 77k to 250k. The cryostat was placed on a 3-d stage which allowed motion in all three axis, this made directing the laser spot to individual devices on the sample much more practical and convenient. A voltage source was connected through channels of the cryostat which allowed for bias voltage to be applied to the individual devices. This bias voltage was swept in 0.1 V steps from -5 to 1 V to find a strong photocurrent response. The voltage measured by the lock in amplifier as the bias voltage was swept was used to determine the photocurrent based on the resistance of circuit which was 50Ω.

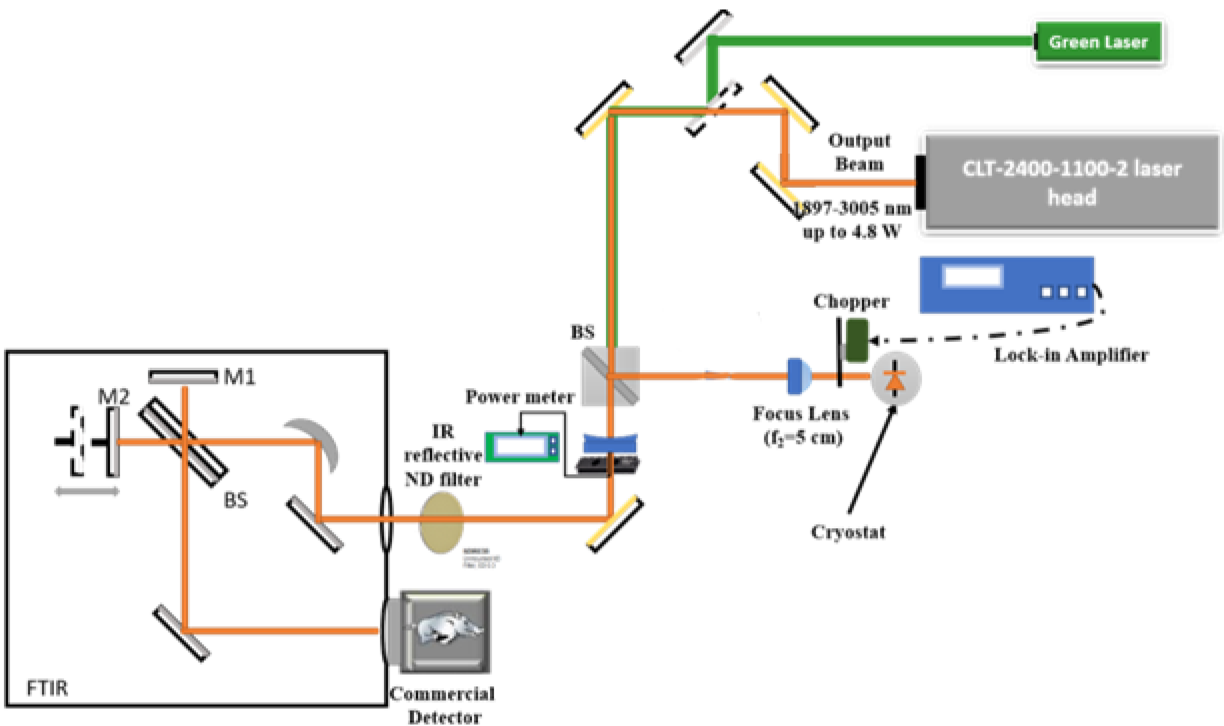

Figure 18- The IPE testing set up, a tunable 3um laser is used with an optical path to excite the sample in a cryostat which the signal is also measured by a power meter and a detector in a FTIR.

4.4 Results and Discussion

The photocurrent was measured in the device while being excited by laser wavelengths from 1.935 um to 2.9 um while under reverse bias. The resulting plot of photocurrent vs. photon energy can be seen in figure 19. Here the photocurrent normalized to the exciting photon energy is equivalent to quantum yield since it is a measure of the number of electrons per exciting photon. From figure 19 it is clear that there are five distinct regions of photocurrent behavior. Region I is the zero-yield region where the photon energy has not exceeded ϕ and no current is able to flow across the interface nor the larger gap material's bandgap. When the threshold ϕ is finally overcome by photon energy region II begins. This region indicates that carriers are being excited from the VBM of the smaller gap GeSn material to the CBM of the larger gap SiGeSn material. The linear extrapolated intersection of region I and II represents the threshold energy ϕ, in this case there were only two data points for region II, so the intersection lies directly on a data point. A smaller step size of the laser wavelength could improve the accuracy of this determination, as it stands ϕ was found to be 0.477 eV.

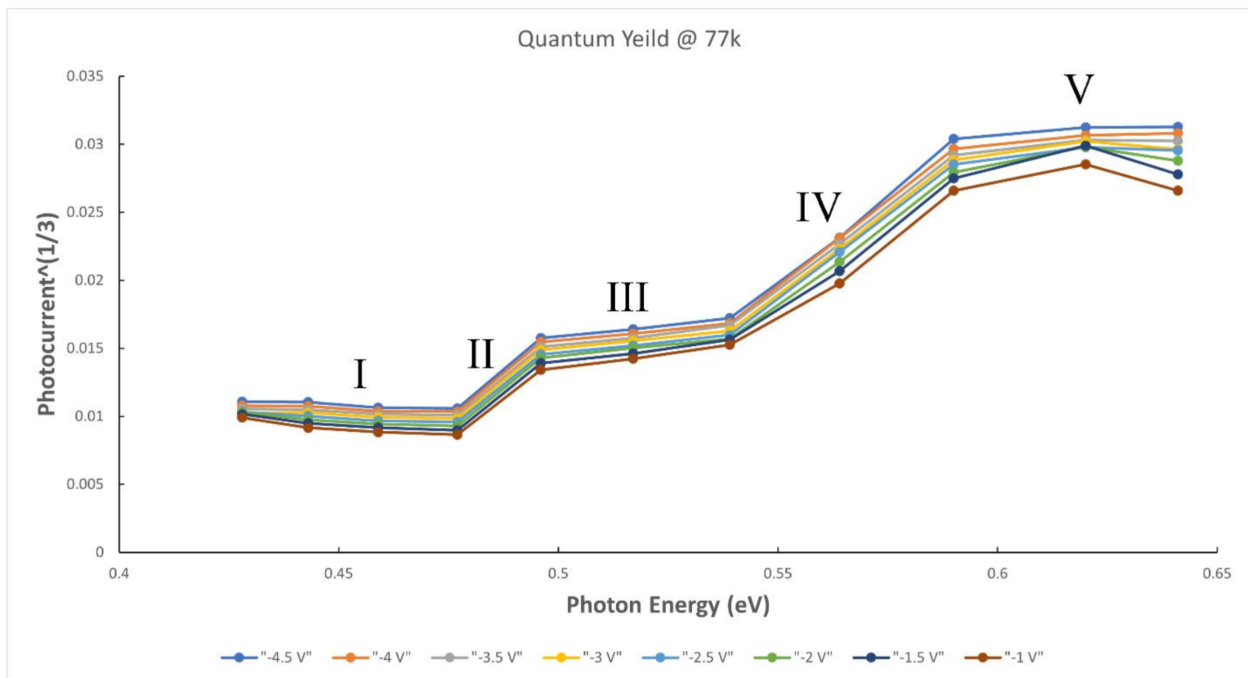

Figure 19 - IPE spectra of FDY-0106 at various bias voltages at 77K

The next region is the point where additional photon energy does not excite additional carriers across the interface yet is still not sufficient to excite carriers directly across the bandgap of SiGeSn. Here region III is effectively the zero-yield region for determining the band gap of the SiGeSn layer. Region IV is when the photon energy is sufficient to excite carriers directly across the larger SiGeSn material bandgap. This continues until region V where further photon energy cannot excite additional carriers and the photocurrent tapers off. The intersection of the linear extrapolation of region III and IV is found to be 0.539 eV and represents the bandgap of the SiGeSn material. From this bandgap value and the threshold energy ϕ the VBO can be calculated simply by subtracting ϕ from the large gap energy. This yields a VBO of 0.062 eV with the VBM of GeSn above (lower energy) the VBM of SiGeSn. The CBO can be determined by measuring the GeSn layer's bandgap by PL and subtracting this energy from the threshold energy ϕ, but these measurements have not been completed at this time.

The IPE spectra shows a stronger response with higher revers bias, as the bias decreases the photocurrent regimes become less linear. In general the biasing did not affect the determination of the threshold energy or bandgap energy as the linear regions and zero-yield regions shift by similar amounts, this has been observed in other IPE papers as well[43]. Similar trends were seen in the IPE data at higher temperatures 100 K, 150 K, 200 K and 250 K, unfortunately the lower photon energies at waves lengths above 2.8 μm did not generate measurable photocurrent which further limited the linear extrapolation of region I, the zero-yield region.

Chapter 5 Conclusions & Future Work

5.1 Conclusions

Two techniques have been demonstrated to empirically determine band offsets between GeSn/Ge and SiGeSn/GeSn, measurements that are otherwise undocumented in literature. The XPS data suggests a small VBO (0.02-0.09 eV) between $Ge_{0.9}Sn_{0.1}$ and Ge with the VBM of the Ge buffer slightly above the VBM of GeSn. Here the quality of instrumentation and accuracy of the VBE determination could be improved to build more confidence in the repeatability and reliability of this measurement. Additionally, the impact on strain influencing the VBE requires additional investigation as the influence was shown to be none trivial in the Ge/Si interface and may also play a role in the GeSn/Ge interface.

The IPE technique was used to determine a small VBO of 0.062 eV at the $Ge_{0.882}Sn_{0.118}/Si_{0.024}Ge_{0.892}Sn_{0.084}$ interface with the SiGeSn VBM above the GeSn VBM suggesting a type-I band alignment. Additional data collection with smaller excitation energy step size could improve the accuracy of this measurement. Determining the bandgaps of both the GeSn and SiGeSn layer through PL would increase the confidence of this determination by confirming the SiGeSn bandgap is accurate. With the GeSn bandgap the CBO can also be determined which would complete the characterization of the band structure for this particular composition.

5.2 Future Work

The challenges involved with accurate empirical determination of band offsets in semiconductor heterojunctions are definitely non-trivial. The work presented here has laid the foundation for repeatable offset determination in GeSn and SiGeSn material systems. Going forwards the IPE measurement technique seems more promising for offset determination because the measurement is not affected by sample strain and does not have to determine the position of the VBE which proves challenging in the XPS method. Improving the IPE results on FDY-0106 is the logical first step. A smaller wavelength step will yield a more accurate value for the threshold energy and bandgap of SiGeSn while will improve the VBO accuracy in turn. Additionally, the bandgap values of the SiGeSn and GeSn layers should be determined by PL to further strengthen the confidence in the technique.

Currently it is planned to perform additional measurements to further increase the confidence of the IPE results and potentially develop the XPS technique. For IPE dark current measurements will be performed on FDY-0106 to ensure that the measured photocurrent is a result of the expected transitions and not influenced by thermal effects. The bandgap values will also be measured by alternative methods such as ellipsometry to add more confidence in this value which can confirm the accuracy of the IPE determination. Furthermore, the band energy structure of the whole sample will be investigated to better understand all regions in the IPE spectrum of figure 19. For XPS using an alternate system of one of our collaborators is the most reasonable method to improve the quality since the vacuum level of our system is lacking. Additionally investigating the effects of strain on the VBE is necessary to ensure that the effects of strain are accounted for in the offset determination.

Once the analysis of FDY-0106 is concluded additional sample compositions should be

fabricated and characterized by IPE. Developing a data base of band offsets for different compositions will be a valuable resource that could identify trends in the offsets based on material compositions allowing for better modeling of yet unachieved material compositions. The IPE set up could be upgraded with additional photon sources such as a free electron laser which would allow direct measurement of CBO energy without the need for PL of the smaller bandgap material's energy gap. Other photon sources with more range would also benefit the set up since the energies beyond 2.8 um were difficult to measure at temperatures above 77 K although this could be related to the quality of FDY-0106. Once the offsets are well understood the long-term goal would be using the offsets for modeling, design and fabrication of GeSn and SiGeSn photodetectors and eventually IR cameras.

Bibliography

[1] I. Yonenaga, "Germanium crystals," in *Single Crystals of Electronic Materials*, Elsevier, 2019, pp. 89–127. doi: 10.1016/B978-0-08-102096-8.00004-5.
[2] M. Fox, *Optical properties of solids*. Oxford ; New York: Oxford University Press, 2001.
[3] P. Y. Yu and M. Cardona, *Fundamentals of semiconductors: physics and materials properties*, 4th ed. Berlin ; New York: Springer, 2010.
[4] Y. Martin *et al.*, "Flip-Chip III-V-to-Silicon Photonics Interfaces for Optical Sensor," in *2019 IEEE 69th Electronic Components and Technology Conference (ECTC)*, Las Vegas, NV, USA, May 2019, pp. 1060–1066. doi: 10.1109/ECTC.2019.00166.
[5] H. Yang *et al.*, "Transfer-printed stacked nanomembrane lasers on silicon," *Nat. Photonics*, vol. 6, no. 9, pp. 615–620, Sep. 2012, doi: 10.1038/nphoton.2012.160.
[6] A. W. Fang, H. Park, O. Cohen, R. Jones, M. J. Paniccia, and J. E. Bowers, "Electrically pumped hybrid AlGaInAs-silicon evanescent laser," *Opt. Express*, vol. 14, no. 20, p. 9203, 2006, doi: 10.1364/OE.14.009203.
[7] S. A. Ghetmiri *et al.*, "Direct-bandgap GeSn grown on silicon with 2230 nm photoluminescence," *Appl. Phys. Lett.*, vol. 105, no. 15, p. 151109, Oct. 2014, doi: 10.1063/1.4898597.
[8] D. W. Jenkins and J. D. Dow, "Electronic properties of metastable Ge x Sn 1 − x alloys," *Phys. Rev. B*, vol. 36, no. 15, pp. 7994–8000, Nov. 1987, doi: 10.1103/PhysRevB.36.7994.
[9] S.-Q. Yu *et al.*, "Development of SiGeSn Technique towards Integrated Mid-Infrared Photonics Applications," in *2019 IEEE BiCMOS and Compound semiconductor Integrated Circuits and Technology Symposium (BCICTS)*, Nashville, TN, USA, Nov. 2019, pp. 1–5. doi: 10.1109/BCICTS45179.2019.8972759.
[10] D. Richter, A. Fried, B. P. Wert, J. G. Walega, and F. K. Tittel, "Development of a tunable mid-IR difference frequency laser source for highly sensitive airborne trace gas detection," *Appl. Phys. B Lasers Opt.*, vol. 75, no. 2–3, pp. 281–288, Sep. 2002, doi: 10.1007/s00340-002-0948-y.
[11] S. Su *et al.*, "GeSn p-i-n photodetector for all telecommunication bands detection," *Opt. Express*, vol. 19, no. 7, p. 6400, Mar. 2011, doi: 10.1364/OE.19.006400.
[12] H. Tran *et al.*, "Si-Based GeSn Photodetectors toward Mid-Infrared Imaging Applications," *ACS Photonics*, vol. 6, no. 11, pp. 2807–2815, Nov. 2019, doi: 10.1021/acsphotonics.9b00845.
[13] F. A. Trumbore, "Solid Solubilities and Electrical Properties of Tin in Germanium Single Crystals," *J. Electrochem. Soc.*, vol. 103, no. 11, p. 597, 1956, doi: 10.1149/1.2430167.
[14] W.-J. Yin, X.-G. Gong, and S.-H. Wei, "Origin of the unusually large band-gap bowing and the breakdown of the band-edge distribution rule in the Sn x Ge 1 − x alloys," *Phys. Rev. B*, vol. 78, no. 16, p. 161203, Oct. 2008, doi: 10.1103/PhysRevB.78.161203.
[15] R. Al-Saigh, M. Baira, B. Salem, and B. Ilahi, "Design of Strain-Engineered GeSn/GeSiSn Quantum Dots for Mid-IR Direct Bandgap Emission on Si Substrate," *Nanoscale Res. Lett.*, vol. 13, no. 1, p. 172, Dec. 2018, doi: 10.1186/s11671-018-2587-1.
[16] S. Wirths *et al.*, "Reduced Pressure CVD Growth of Ge and $Ge_{1-x}Sn_x$ Alloys," *ECS J. Solid State Sci. Technol.*, vol. 2, no. 5, pp. N99–N102, 2013, doi: 10.1149/2.006305jss.
[17] J. Zheng *et al.*, "Growth of high-Sn content (28%) GeSn alloy films by sputtering epitaxy," *J. Cryst. Growth*, vol. 492, pp. 29–34, Jun. 2018, doi: 10.1016/j.jcrysgro.2018.04.008.

[18] S. Zaima, O. Nakatsuka, N. Taoka, M. Kurosawa, W. Takeuchi, and M. Sakashita, "Growth and applications of GeSn-related group-IV semiconductor materials," *Sci. Technol. Adv. Mater.*, vol. 16, no. 4, p. 043502, Jul. 2015, doi: 10.1088/1468-6996/16/4/043502.
[19] J. L. Liu, S. Tong, Y. H. Luo, J. Wan, and K. L. Wang, "High-quality Ge films on Si substrates using Sb surfactant-mediated graded SiGe buffers," *Appl. Phys. Lett.*, vol. 79, no. 21, pp. 3431–3433, Nov. 2001, doi: 10.1063/1.1421092.
[20] J. Margetis *et al.*, "Growth and Characterization of Epitaxial Ge $_{1-X}$ Sn $_{x}$ Alloys and Heterostructures Using a Commercial CVD System," *ECS Trans.*, vol. 64, no. 6, pp. 711–720, Aug. 2014, doi: 10.1149/06406.0711ecst.
[21] J. Rathore, A. Nanwani, S. Mukherjee, S. Das, O. Moutanabbir, and S. Mahapatra, "Composition uniformity and large degree of strain relaxation in MBE-grown thick GeSn epitaxial layers, containing 16% Sn," *J. Phys. Appl. Phys.*, vol. 54, no. 18, p. 185105, May 2021, doi: 10.1088/1361-6463/abe1e8.
[22] E. T. Yu, J. O. McCaldin, and T. C. McGill, "Band Offsets in Semiconductor Heterojunctions," in *Solid State Physics*, vol. 46, Elsevier, 1992, pp. 1–146. doi: 10.1016/S0081-1947(08)60397-5.
[23] G. Di Liberto and G. Pacchioni, "Band offset in semiconductor heterojunctions," *J. Phys. Condens. Matter*, vol. 33, no. 41, p. 415002, Oct. 2021, doi: 10.1088/1361-648X/ac1620.
[24] M. Jaros, "Simple analytic model for heterojunction band offsets," *Phys. Rev. B*, vol. 37, no. 12, pp. 7112–7114, Apr. 1988, doi: 10.1103/PhysRevB.37.7112.
[25] G. Sun, R. A. Soref, and H. H. Cheng, "Design of an electrically pumped SiGeSn/GeSn/SiGeSn double-heterostructure midinfrared laser," *J. Appl. Phys.*, vol. 108, no. 3, p. 033107, Aug. 2010, doi: 10.1063/1.3467766.
[26] S.-W. Chang and S. L. Chuang, "Theory of Optical Gain of ${\hbox {Ge--}}{\hbox {Si}}_{x}{\hbox {Ge}}_{y}{\hbox {Sn}}_{1-x-y}$ Quantum-Well Lasers," *IEEE J. Quantum Electron.*, vol. 43, no. 3, pp. 249–256, Mar. 2007, doi: 10.1109/JQE.2006.890401.
[27] J. Menéndez and J. Kouvetakis, "Type-I Ge∕Ge1−x−ySixSny strained-layer heterostructures with a direct Ge bandgap," *Appl. Phys. Lett.*, vol. 85, no. 7, pp. 1175–1177, Aug. 2004, doi: 10.1063/1.1784032.
[28] S. Wirths *et al.*, "SiGeSn growth studies using reduced pressure chemical vapor deposition towards optoelectronic applications," *Thin Solid Films*, vol. 557, pp. 183–187, Apr. 2014, doi: 10.1016/j.tsf.2013.10.078.
[29] P. Moontragoon *et al.*, "Electronic properties calculation of Ge1−x−ySixSny ternary alloy and nanostructure," *J. Non-Cryst. Solids*, vol. 358, no. 17, pp. 2096–2098, Sep. 2012, doi: 10.1016/j.jnoncrysol.2012.01.025.
[30] H. Kroemer, "Determination of heterojunction band offsets by capacitance-voltage profiling through nonabrupt isotype heterojunctions," *Appl. Phys. Lett.*, vol. 46, no. 5, pp. 504–505, Mar. 1985, doi: 10.1063/1.95572.
[31] F. Seitz and H. Ehrenreich, Eds., *Solid state physics: advances in research and applications. Vol. 46*, vol. 46. New York, NY: Academic Press, 1992.
[32] S. Tongay, M. Lemaitre, X. Miao, B. Gila, B. R. Appleton, and A. F. Hebard, "Rectification at Graphene-Semiconductor Interfaces: Zero-Gap Semiconductor-Based Diodes," *Phys. Rev. X*, vol. 2, no. 1, p. 011002, Jan. 2012, doi: 10.1103/PhysRevX.2.011002.
[33] J. Baur, K. Maier, M. Kunzer, U. Kaufmann, and J. Schneider, "Determination of the GaN/AlN band offset via the (-/0) acceptor level of iron," *Appl. Phys. Lett.*, vol. 65, no. 17, pp. 2211–2213, Oct. 1994, doi: 10.1063/1.112764.

[34] M. Kira and S. W. Koch, *Semiconductor Quantum Optics*. Cambridge: Cambridge University Press, 2011. doi: 10.1017/CBO9781139016926.

[35] O. Ostinelli, G. Almuneau, and W. Bächtold, "Photoluminescence and band offset of type-II AlGaAsSb/InP heterostructures," *Semicond. Sci. Technol.*, vol. 21, no. 5, pp. 681–685, May 2006, doi: 10.1088/0268-1242/21/5/020.

[36] C. J. Chen, *Introduction to scanning tunneling microscopy*. New York: Oxford University Press, 1993.

[37] E. L. Wolf, *Principles of electron tunneling spectroscopy*, 2nd ed. Oxford ; New York: Oxford University Press, 2012.

[38] R. M. Feenstra, "Tunneling spectroscopy of the (110) surface of direct-gap III-V semiconductors," *Phys. Rev. B*, vol. 50, no. 7, pp. 4561–4570, Aug. 1994, doi: 10.1103/PhysRevB.50.4561.

[39] J. F. Watts and J. Wolstenholme, *An introduction to surface analysis by XPS and AES*. Chichester, West Sussex, England ; New York: J. Wiley, 2003.

[40] P. Van der Heide, *X-ray photoelectron spectroscopy: an introduction to principles and practices*. Hoboken, N.J: Wiley, 2012.

[41] J. S. Helman and F. Sánchez-Sinencio, "Theory of Internal Photoemission," *Phys. Rev. B*, vol. 7, no. 8, pp. 3702–3706, Apr. 1973, doi: 10.1103/PhysRevB.7.3702.

[42] V. V. Afanas'ev and A. Stesmans, "Internal photoemission at interfaces of high-κ insulators with semiconductors and metals," *J. Appl. Phys.*, vol. 102, no. 8, p. 081301, Oct. 2007, doi: 10.1063/1.2799091.

[43] C. Coluzza *et al.*, "Interface measurements of heterojunction band lineups with the Vanderbilt free-electron laser," *Phys. Rev. B*, vol. 46, no. 19, pp. 12834–12836, Nov. 1992, doi: 10.1103/PhysRevB.46.12834.

[44] J. T. McKinley, "Free-electron laser internal photoemission measurements of heterojunction band discontinuities," *J. Vac. Sci. Technol. B Microelectron. Nanometer Struct.*, vol. 11, no. 4, p. 1614, Jul. 1993, doi: 10.1116/1.586979.

[45] V. V. Afanas′ev, *Internal photoemission spectroscopy: fundamentals and recent advances*, 2nd ed. London: Elsevier, 2014.

[46] E. A. Kraut, R. W. Grant, J. R. Waldrop, and S. P. Kowalczyk, "Precise Determination of the Valence-Band Edge in X-Ray Photoemission Spectra: Application to Measurement of Semiconductor Interface Potentials," *Phys. Rev. Lett.*, vol. 44, no. 24, pp. 1620–1623, Jun. 1980, doi: 10.1103/PhysRevLett.44.1620.

[47] T. E. Cook, C. C. Fulton, W. J. Mecouch, R. F. Davis, G. Lucovsky, and R. J. Nemanich, "Band offset measurements of the Si3N4/GaN (0001) interface," *J. Appl. Phys.*, vol. 94, no. 6, pp. 3949–3954, Sep. 2003, doi: 10.1063/1.1601314.

[48] S. C. Su *et al.*, "Valence band offset of ZnO/Zn0.85Mg0.15O heterojunction measured by x-ray photoelectron spectroscopy," *Appl. Phys. Lett.*, vol. 93, no. 8, p. 082108, Aug. 2008, doi: 10.1063/1.2977478.

[49] S. A. Ding *et al.*, "Valence band discontinuity at a cubic GaN/GaAs heterojunction measured by synchrotron-radiation photoemission spectroscopy," *Appl. Phys. Lett.*, vol. 70, no. 18, pp. 2407–2409, May 1997, doi: 10.1063/1.118886.

[50] T. Kitatani, M. Kondow, T. Kikawa, Y. Yazawa, M. Okai, and K. Uomi, "Analysis of Band Offset in GaNAs/GaAs by X-Ray Photoelectron Spectroscopy," *Jpn. J. Appl. Phys.*, vol. 38, no. Part 1, No. 9A, pp. 5003–5006, Sep. 1999, doi: 10.1143/JJAP.38.5003.

[51] W. F. Zhang, T. Nishimula, K. Nagashio, K. Kita, and A. Toriumi, "Conduction band offset at GeO $_2$ /Ge interface determined by internal photoemission and charge-corrected x-

ray photoelectron spectroscopies," *Appl. Phys. Lett.*, vol. 102, no. 10, p. 102106, Mar. 2013, doi: 10.1063/1.4794417.

[52] J. R. Waldrop, R. W. Grant, S. P. Kowalczyk, and E. A. Kraut, "Measurement of semiconductor heterojunction band discontinuities by x-ray photoemission spectroscopy," *J. Vac. Sci. Technol. Vac. Surf. Films*, vol. 3, no. 3, pp. 835–841, May 1985, doi: 10.1116/1.573326.

[53] M. K. Hudait, Y. Zhu, N. Jain, and J. L. Hunter, "Structural, morphological, and band alignment properties of GaAs/Ge/GaAs heterostructures on (100), (110), and (111)A GaAs substrates," *J. Vac. Sci. Technol. B Nanotechnol. Microelectron. Mater. Process. Meas. Phenom.*, vol. 31, no. 1, p. 011206, Jan. 2013, doi: 10.1116/1.4770070.

[54] G. P. Schwartz, M. S. Hybertsen, J. Bevk, R. G. Nuzzo, J. P. Mannaerts, and G. J. Gualtieri, "Core-level photoemission measurements of valence-band offsets in highly strained heterojunctions: Si-Ge system," *Phys. Rev. B*, vol. 39, no. 2, pp. 1235–1241, Jan. 1989, doi: 10.1103/PhysRevB.39.1235.

[55] E. T. Yu, "Measurement of the valence band offset in novel heterojunction systems: Si/Ge (100) and AlSb/ZnTe (100)," *J. Vac. Sci. Technol. B Microelectron. Nanometer Struct.*, vol. 8, no. 4, p. 908, Jul. 1990, doi: 10.1116/1.584941.

[56] G. S. May and C. J. Spanos, *Fundamentals of semiconductor manufacturing and process control*. [Piscataway] : Hoboken, N.J: IEEE ; Wiley-Interscience, 2006.